Fatigue crack growth retardation and acceleration in coupon specimens and tubular joint element specimens

R.J.M. Pijpers, S.A. Verdenius, L.M. Abspoel-Bukman, J. Maljaars
TNO, Structural Reliability

This experimental study considers load sequence effects in fatigue crack growth in coupon specimens and in element specimens. The coupon specimens were standard edge crack configurations cyclically loaded under four point bending on base metal and welds, whereas the element specimens were full-scale axially loaded tubular joints. Whereas load sequence effects such as crack growth retardation following high stress peaks (overloads) in base metal are already known, this paper makes a qualitative comparison to more realistic conditions of random variable amplitude loading and welded joints. The results of the coupon specimens show that the crack growth retards following an overload or a block of ranges with high mean stress in a further constant amplitude load regime for the steel grades investigated, whereas an underload applied after an overload reduces or cancels out the retarding effect. Test results on full scale tubular joint elements show that in case of realistic load sequences on realistic structural details, the net effect of overloads and underloads on the crack growth rate measured over the entire life is insignificant. As the majority of the fatigue life consists of growth of small cracks, the limited significance of load sequences is attributed to the limited crack growth experienced between events such as storms, so that retardation effects do not have the possibility to fully develop and are cancelled out by underloads. On the other hand, load sequence effects appear more significant for large cracks - and hence for inspections - in realistic joints as compared to coupon specimens.

Key words: Fatigue, experiments, tubular joint, crack growth rate, crack growth retardation, load sequence effect, overload, variable amplitude

1 Introduction

Offshore wind turbine (OWT) structures and their foundations such as jackets and monopiles are prone to fluctuating loads with a variable amplitude. The fatigue life of welded joints is an important design driver influencing capital expenditure as well as

operational expenditure because of inspections and repairs. In the design stage, fatigue damage is typically calculated by the Palmgren-Miner rule of linear cumulative damage using S-N curves as provided in standards such as Eurocode, DNV-GL and IIW. This approach does not consider load sequence effects. The sequence of the loading, however, potentially influences the fatigue crack growth rate.

An example of a load sequence effect is an incidental large stress peak or overload (OL) in a further constant amplitude (CA) loaded specimen that effectively retards crack growth. An explanation for the retardation of the crack growth after an OL is that retardation occurs due to residual plastic elongation induced crack closure at the crack flanks in the plastic zone, See Figure 1. Newman (1981, 1982, 1984) shows that the effect of an OL with crack closure is that the stress needed to re-open a crack in subsequent cycles is substantially larger than the crack opening stress at an equivalent CA load, without having a prior OL. An OL therefore reduces the effective stress intensity range in the crack tip and thus decreases the crack growth rate.

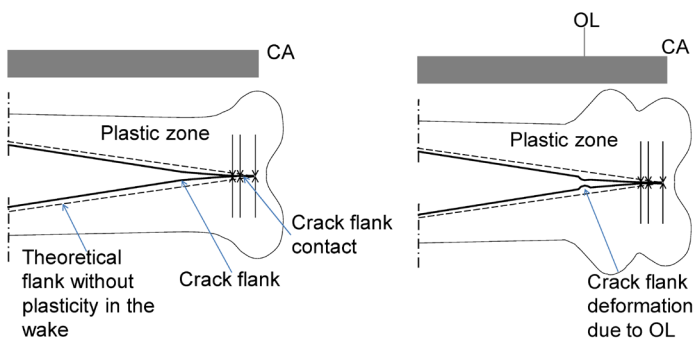

Crack closure in constant amplitude loading (CA)

Crack closure in case of an overload (OL)

Figure 1: Crack closure [Maljaars & Tang, 2020]

Observed and reported phenomena of fatigue crack growth and acceleration due to load sequences are known for decades, and generally part of standard textbooks on fatigue, such as Schijve (2009). However, limited data is available in literature regarding load sequence effects on the crack growth of welded structural steel components, that are largely influenced by tensile residual stress as a result of thermal cycling and that may have an inhomogeneous material structure. Tests on thick-walled welded steel specimens in Lim & Stephens (1990) show significant retardation effects in case of large OL. Crack

growth retardation has also been found in thick-walled C–Mn steel specimens subjected to a variable amplitude (VA) load, given in Noordhoek (1997), Zheng et al. (1994) and Fischer et al. (1983). Salvati et al. (2017) considered the combined effects of crack closure and residual stress in crack growth retardation due to an overload. They did this by performing tests with low and with high stress ratio. Maljaars et al. (2015) provide the results of an experimental programme, where retardation effects and VA effects are monitored on a single batch of material. Significant retardation effects were observed in as-welded specimens even though the opening stress was (almost) equal to the minimum stress of the cycles. Although limited data is available of the effect of single load events on welded structural steels, clear quantification of load sequence effects in welded connections is still missing especially for realistic VA loads. Therefore, in the project FeLoSEFI, fatigue life prediction models are developed, that include load sequence effects, specifically focusing on offshore structures. If the influence of load sequence effects is significant, further nuance could be incorporated in design and maintenance standards regarding fatigue and S-N curves could be derived or adapted specifically for certain load combinations.

Aim of the current paper is to assess load sequence effects in coupon specimens that are usually considered for this purpose and tubular joint element specimens with realistic loading as obtained in practical conditions. The paper presents experimental work on fatigue crack growth behaviour as observed in both coupon specimens and tubular joint element specimens. Coupon specimens were single edge notched four-point-bending (SENB4) specimens made of base material S355G10+M and S460M, and welded connections thereof with matching weld material strength, in which the crack growth rate is determined. Tubular joint element specimens were made of structural steels S355J2H and S355G13+N as brace and chord material, and the elements are representative for a regularly applied joint in a simplified jacket structure of an offshore wind turbine foundation. Both coupons as well as element specimens were considered in this study as the advantage of the coupons is that crack growth through thickness can be monitored in detail, whereas the tubular joint elements have more realistic residual stress conditions and inherently incorporate size effects, which appear relevant for fatigue of this type of joint [Lotsberg, 2014]. The test loading contained constant amplitudes, discrete over- and underloads, and realistic loading histories based on monitoring data of existing wind farms in the Netherlands. The used monitoring data provide insight into the effect of realistic structural loading history on the crack growth rate and thereby the fatigue life. An

important feature in the load sequences in offshore wind turbines is the mean shift caused by the changing wind directions, which was incorporated in the experiments.
The paper intends to provide background to standardisation (i.e. Eurocode, DNV-GL, IIW), and therefore focuses on qualitatively understanding crack growth behaviour, which will influence eventual S-N curves, instead of giving a very detailed description of the load sequence effects and all relevant stages of crack growth. The experimental results in the paper were used for validation of fatigue crack growth models, presented in Maljaars et al. (2020) and Dragt et al. (2020), in which a more elaborate description of relevant influence parameters is given to describe the crack growth behaviour for complex geometries and load sequences.

2 Coupon specimen experiments

2.1 Experimental program

The coupon specimens are single edge notched four-point bending (SENB4) test samples made of base material and flux core arc welded specimens: K-welds and bead-on-plate welds. Coupon specimens of full height were cut from the base material and welded plates. The top and bottom sides of the welded specimens were ground flush in order to remove weld caps so as to prevent influence of this geometrical discontinuity on the crack growth rate. An initial defect was milled with nominal depth of 2 mm by using electric discharging (EDM). The notch was applied over the full width of the specimens (perpendicular to the rolling direction) at midspan of the specimens.

The following parameters are assessed in detail: 1) effect of load cycles on the crack growth rate a) constant amplitude loading providing the reference for the determination of crack growth parameters (da/dN as a function of ΔK); b) constant amplitude fatigue loading with overloads (OLs) and underloads (ULs) at discrete time steps; c) random variable loading (VAR) and block loading (VASB); 2) effect of residual stresses a) base material (unwelded) S355GM+M (50 mm thick) versus S460M (40 mm thick); b) bead-on-plate welded joints with residual stresses; c) K-welded joint with residual stresses; d) stress relieved bead-on-plate welded joint.

CA tests with OL and UL

In the constant amplitude tests, the maximum and minimum load were kept constant during the test. Five different stress ratios R ($=\sigma_{min}/\sigma_{max}$) values were applied in these tests:

R = 0.1, 0.3, 0.5, 0.6 and 0.7. In some tests, at specific number of cycles, an incidental OL or UL was applied. The overload event was in some cases directly followed by an underload (OL+UL).

Variable Amplitude Random tests

Several specimens were tested using a scaled and filtered version the measurement signal from an existing dataset containing field measurements on an existing offshore wind foundation [Dragt & Allaix, 2019]. First, the original input was scaled by multiplying the signal with a fixed factor so that the capacity of the test setup (600 kN) was not exceeded. This resulted into a maximum stress range is 400 MPa. Second, a rainflow cycle counting procedure was applied and all cycles with ranges smaller than 70 MPa were removed. This significantly reduced testing time, whereas the effect on the total fatigue damage or crack growth due to these cycles was negligibly small. This results in the signal shown in Figure 2. This signal is continuously repeated in the test.

Variable Amplitude Stress Blocks tests

In addition to the variability of the stress cycles due to the wind gusts of various magnitude, wind turbines are subject to changes in the mean stress level caused by changes in the wind direction [Dragt & Allaix, 2019]. To test the effect of mean changes on the crack growth rate, several specimens were tested using a block scheme.

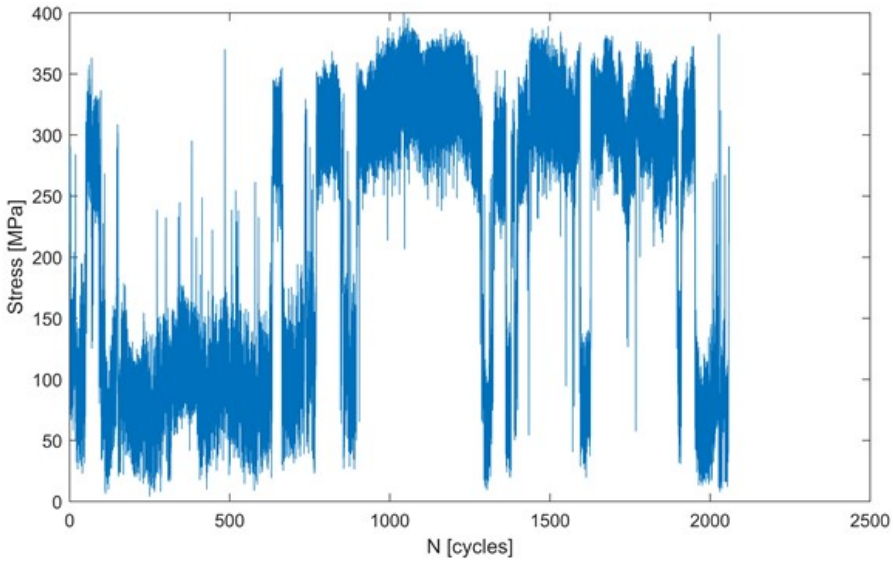

Stress history in coupon test

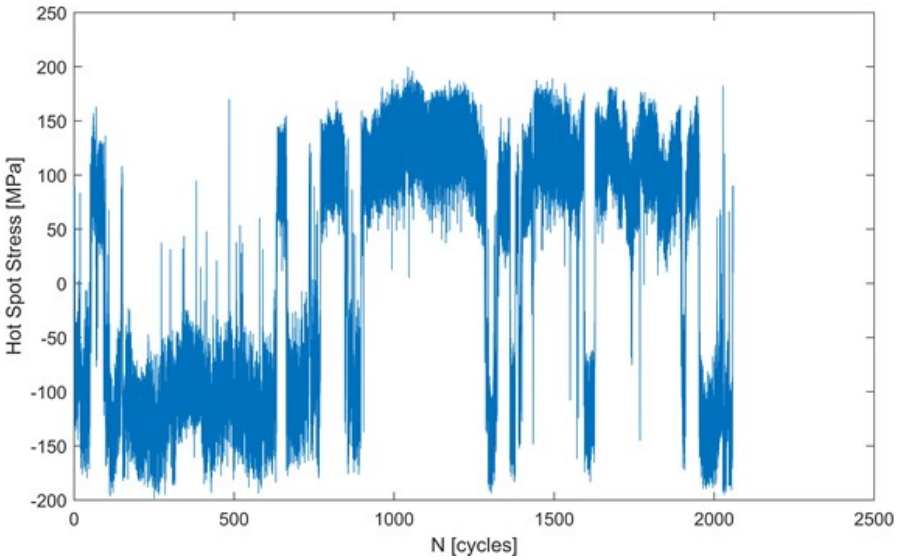

(Hot spot) stress history in tubular joint element tests

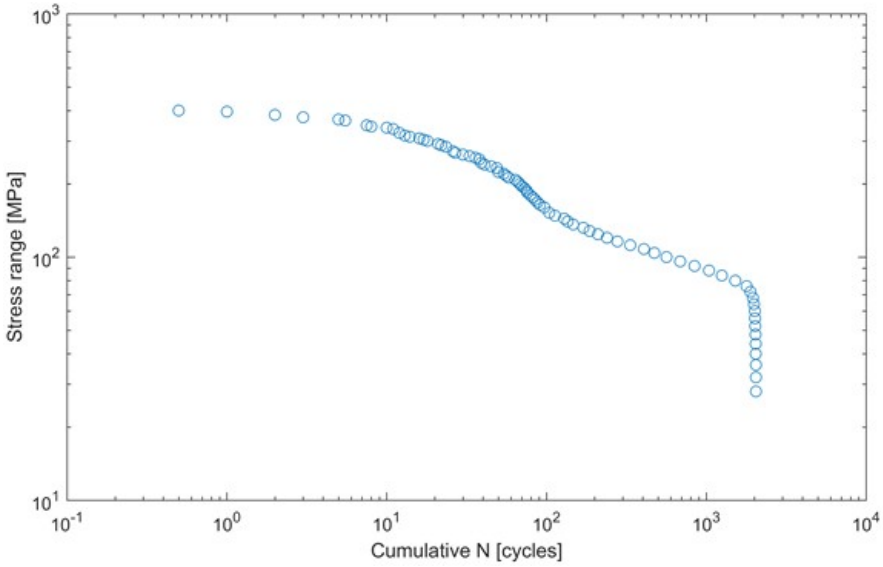

Stress range spectrum derived from stress history

(Similar for tubular joint element test and coupon test)

Figure 2: Variable amplitude random (VAR) signal (repeated in test)

One example of a block loading is given in Figure 3 which shows the stress over number of cycles, for one test. Every block except from the single overload is tuned in such a way that

it represents approximately 1 mm of crack growth, which was determined with a simplified fracture mechanics model and crack growth properties from literature. This 1 mm crack extension allows to measure the effect of the overload and mean changes on the crack growth before a subsequent block is applied. Table 1 summarises the variables of the crack growth tests.

2.2 *Test rig, specimens and instrumentation*

Two four-point bending setups with cylinder capacity 350 kN were built in the TNO Structural Dynamics Lab in Delft. The test frequency was 4 Hz but the tests were periodically stopped to allow for measurements. Rolling supports and hinges were manufactured to obtain the correct boundary conditions in the specimen. Figure 4 shows the details of the standard four-point single-edge-notch bend, SENB4, specimen with a height of 50 mm and width of 25 mm (S355G10+M), for which reference is given in ASTM E647-15e1:2015 and ISO12108:2012. The specimens of S460M had a height of 40 mm and a width of 20 mm. As the weld cap was removed in all welded specimens, the height of the welded specimens was prone to a small variation, See Table B2 in Annex B. The applied inner and outer span was typically 140 mm and 280 mm for the S355G10+M specimens

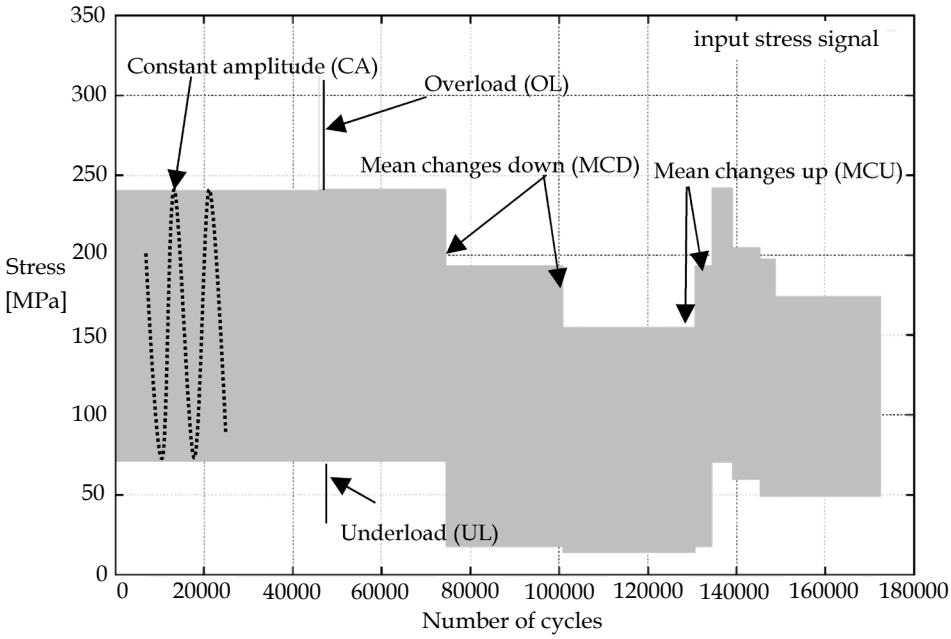

Figure 3: Example of a variable amplitude stress block (VASB) loading signal

Table 1: Variables of the crack growth tests

Material	**Loading**	**Stress ratio *R* (at CA)**
S355G10, 50 mm	Constant amplitude (CA)	0.1
S460M, 40 mm	Mean change down (MCD)	0.3
	Mean change down + up (MCDU)	0.5
Type	Mean change up (MCU)	0.6
Base material (BM)	Overload (OL)	0.7
Bead-on-plate weld (BP)	Overload + direct underload (OL+UL)	
K-weld (KW)	Underload (UL)	
	Variable amplitude random (VAR)	
	Variable amplitude stress blocks (VASB)	

versus 100 mm and 200 mm for the S460M specimens, See Table B2 in Annex B. Some S355G10+M specimens had 100 mm and 200 mm spans as recommended by ASTM E647-15e1:2015. However, as a result of the relatively large overloads in the tests, plastic straining was observed at the supports for these short spans. With the larger span, these problems were overcome.

Instrumentation

Two systems of data acquisition – Teststar with Basic testware – were used for the data acquisition. In software MTS Multipurpose Elite, automated test procedures were built for the variable amplitude testing, in which the load histories were looped.

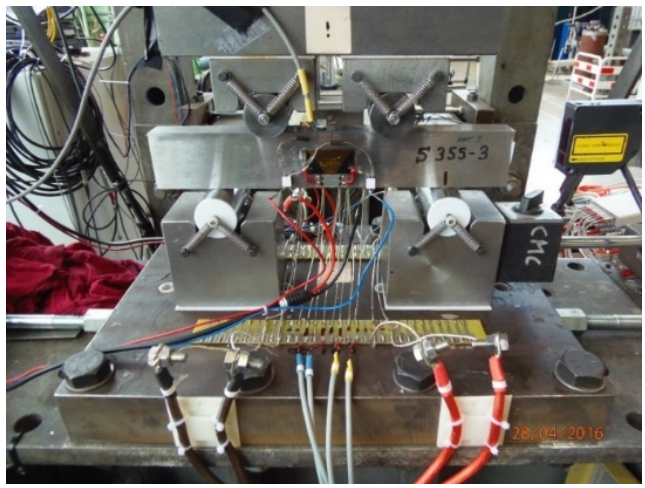

Figure 4: SENB4 specimen in test rig

Crack depth is monitored during the tests from initial notch size a_i until a_f with the corresponding number of cycles, N. A number of visual and non-visual methods were used to determine the crack depth: crack gauges, back face strain gauges and visual observation by camera with zoom. The crack gauges consist of a pattern of resistor strands (grids) that were connected in parallel. When bonded to a structure, progression of a surface crack through the gage pattern causes successive open-circuiting of the strands, resulting in an increase in total resistance. One of the two following types of crack gauges (or combinations thereof) were used every specimen, See Figure 5: 1) Crack gauge with 10 grid lines with spacing Δa = 0.25 mm between centrelines (type: Vishay), 2) Crack gauge with 40 grid lines with spacing Δa = 0.50 mm between centrelines (type: Sokki).

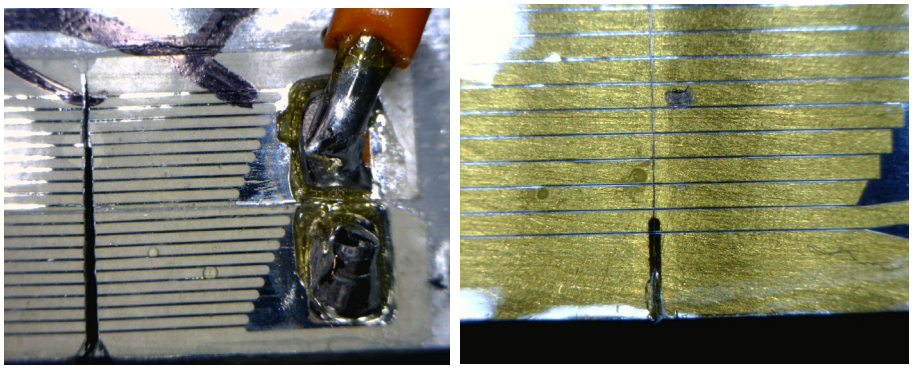

type Vishay *type Sokki*

Figure 5: Crack gauges

Figure 18 and Figure 20 give an example of the measured crack length using the Vishay crack gauges with a spacing of 0.25 mm. Visual observations of the crack depth were made frequently by using handheld microscopic camera Dino Lite type AM-413T, with magnification of 50-200x.

*2.3 **Material characterization***

Base material specimens

Table 2 gives the chemical composition and Table 3 the mechanical properties of the base metal. As the main focus of the paper is on S355G10+M steel, the microstructure of the base material is evaluated for this material with respect to the following aspects that are known to influence the fatigue resistance: homogeneity, residual stress, and grain size. The microstructure is studied using electron microscopy. Segregation layers were not observed

Table 2: Chemical composition (weight %) of the base metal

	C	Mn	Si	S	P	Al	N	Cu	
S355G10+M	0.07	1.51	0.302	0.002	0.013	0.031	0.005	0.228	
S460M	0.11	1.42	0.241	0.001	0.014	0.029	0.0062	0.025	
	Ni	Cr	As	Sn	Mo	Nb	V	Ti	B
S355G10+M	0.21	0.027	0.002	0.002	0.001	0.026	0.001	0.017	0.0002
S460M	0.021	0.03			0.003	0.047	0.035	0.014	

Table 3: Mechanical properties of the base metal

	Ultimate strength	Yield strength	Failure strain	Charpy Toughness	Charpy test temperature
	S_u (MPa)	S_y (MPa)	A_5 (%)	*Cv*	*T* [°C]
S355G10+M	486	380	28.1	178-198	-40
S460M	566	479	24.1	202-204	-20

– the microstructure is homogenic – up to mid thickness. Figure 6 presents the microstructure and it shows alternating bands of pearlite and ferrite in an angle of approximately 8° with the plate surface. This is typical of TM steels and it is caused by the rolling process. A widmanstätten microstructure is visible in mid-thickness.

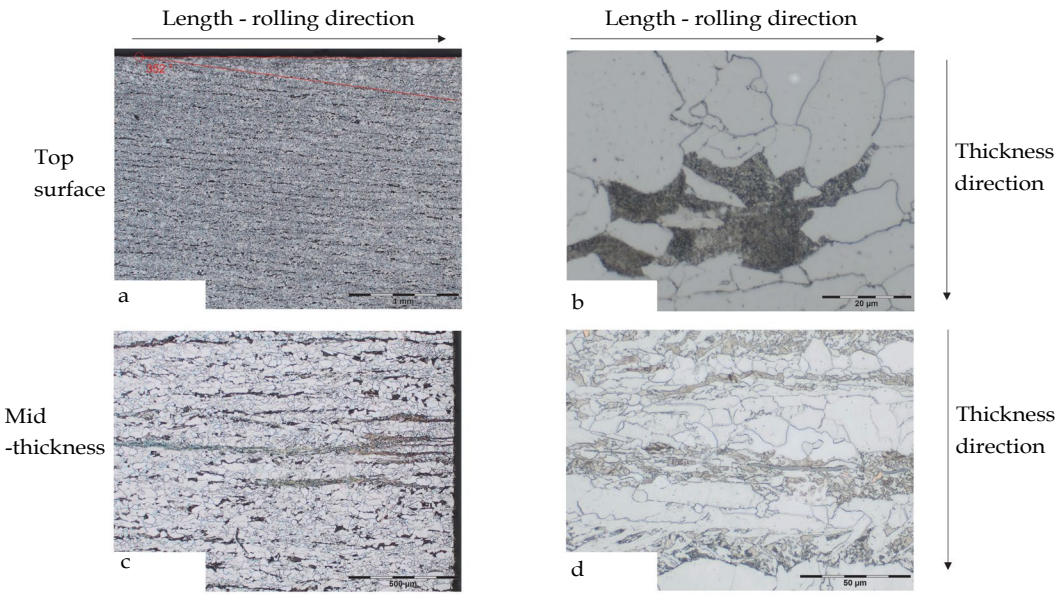

Figure 6: a. Ferrite-pearlite microstructure with pearlite layers in an angle of approximately 8°; b. Pearlite; c./d. Widmanstätten microstructure in mid-thickness

Based on Electron-beam backscattering deflection (EBSD) analysis of the base material at various depths from the surface, the grain orientation spread (GOS) and maximum orientation spread (MOS) maps were determined. These are primary strain analysis tools indicating deformed grains as a heat colour map as well as the spatial distribution and numerical prevalence of grains with certain levels of strain, Figure 7. No crystallographic preference orientation of the grains was observed. From 3 mm to 9 mm from the top surface, the residual stress in the base material increases between 3 mm and 9 mm from the top surface, after which it remains approximately constant. EBSD could not determine if

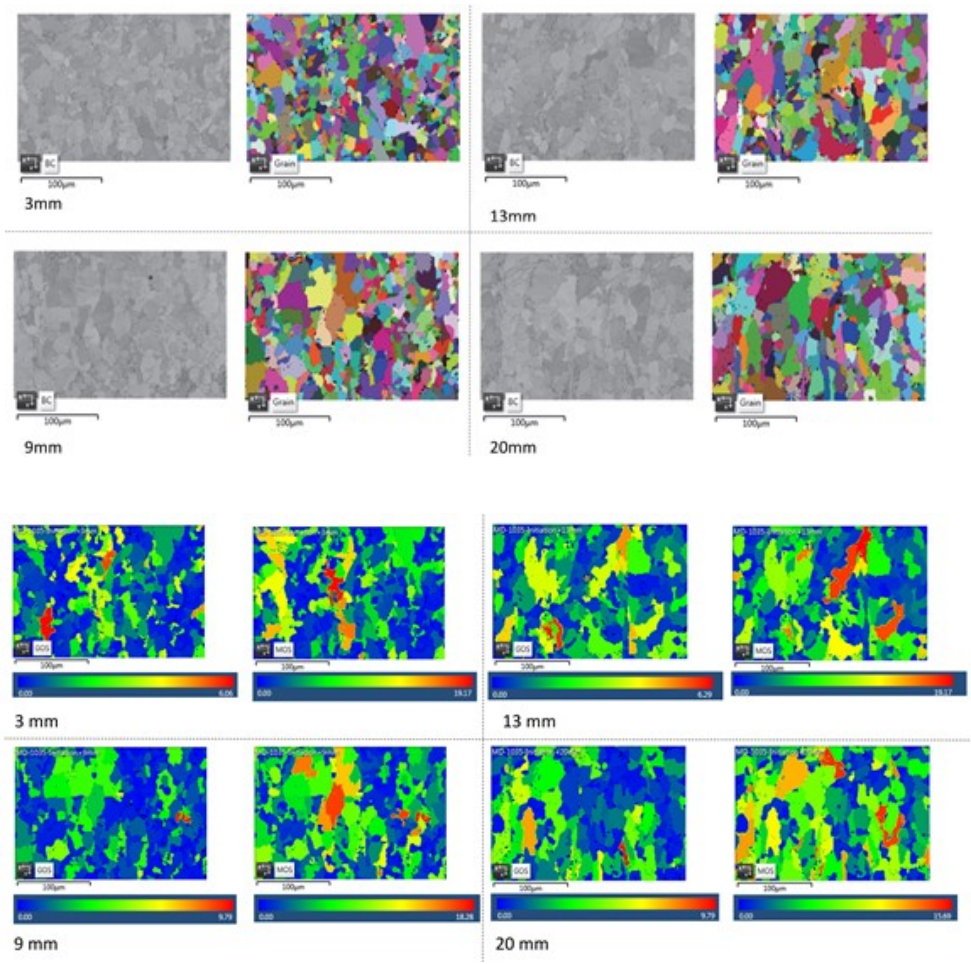

Figure 7: EBSD and grain analysis at four depths from the top surface: 3 mm, 9 mm, 13 mm and 20 mm (half plate thickness is 25 mm)

stress is tensile or compressive but, given the work done through the rolling process, these residual stresses were compressive close to the surfaces. Because residual stresses are self-balancing, this implies that the residual stress were tensile at a larger depth. Table 4 shows that the grain size increases with increasing distance from the plate surface up to a thickness of 13 mm and it remains approximately constant thereafter.

Table 4: Grain size

Depth from surface	Grain Area (μm²)	
	Mean	Standard Deviation
3	84.45	112.7
9	111.32	166.28
13	130.92	192.61
20	138.03	207.95

Welded specimens

The weld caps were ground flush after welding (indicated in grey) to remove weld reinforcing influence on the crack growth rate. K-welds were applied in order to have a heat affected zone (HAZ) along the entire crack path (See Figure 8) and a representative residual stress distribution of a two-sided butt weld. The bead-on-plate welds (with one weld run) had a through thickness transition from weld material to base material. The material transition and residual stress distribution in a bead-on-plate weld is assumed to be representative of a weld connection in a tubular joint, that is typically applied in an offshore jacket. Therefore, a similar weld process (flux core arc welding) was applied in the bead-on-plate weld in the coupon specimens, to the one that is applied in the tubular joint specimens. In the welded specimens, the notch was applied in the fusion line in the HAZ, at the straight side of the K-weld and at one of the sides of the bead-on-plate weld.

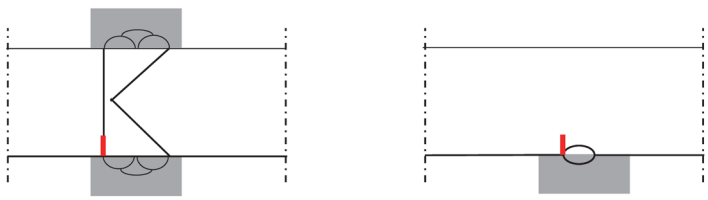

K-weld *Bead-on-plate weld*

Figure 8: Welded specimens with ground edge and crack position in red

Tensile residual stresses present in the outer fibre of the specimens raise the effective stress ratio *R*. A more detailed study of the residual stress profile in the Bead-on-plate specimens is provided in Rikken et al. (2018). Two crack compliance tests were performed on the bead-on-plate welded specimens. The average difference between these two tests was 2% and the difference between the maximum residual stress values was also 2%. Figure 9 presents the residual stress state of one test for plane strain and for plane stress constraint assumptions. The maximum tensile stress is measured in the sub-surface region and is equal to 210 MPa, or 54% of the base material yield stress at room temperature for the plane strain assumption and slightly lower for the plane stress assumption. A balancing compression stress is present in the core. The angular distortion caused by welding provides a tensile stress at the bottom side. The maximum base material residual stress is 7% of the residual stress of the bead-on-plate welded specimen. One specimen with bead-on-plate weld was stress-relieved before loading, by exposure to 560 °C for 70 min after which cooling was performed in air.

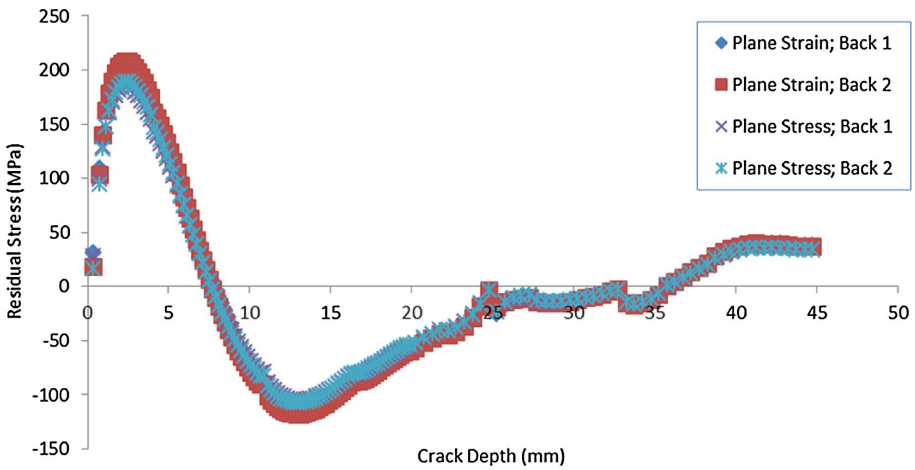

Figure 9: Residual stress of the bead-on-plate welded specimen perpendicular to the weld direction at 2 mm from the weld toe

Residual stress measurements were not performed on the K-welded specimens. Due to the multi-pass welding, the residual stress in K-welded specimens is expected to be more scattered and generally lower as compared to the bead-on-plate specimen. Microstructural examination as for the base metal specimens was not performed on the welded specimens.

2.4 *Crack growth rate and stress intensity range*

The results of the constant amplitude fatigue tests were evaluated in terms of crack depth, a, as a function of number of cycles, N, as well as the crack growth rate, da/dN, as a function of the stress intensity factor, ΔK. The monotonic stress intensity K is a function of the crack geometry and the stress; it represents the stress state at the crack tip. The calculation of the stress intensity range ΔK as a function of stress range and SENB4 geometry is done with the parametric equation of Tada et al. (1973). The derivation of material parameters for crack growth was based on the following – simplified – relation between ΔK and da/dN

$$da/dN = C(R) \cdot \Delta K^M \quad \text{or} \quad \log da/dN = \log C(R) + M (\log \Delta K) \tag{1}$$

where

da/dN = crack growth rate [mm/cycle]

ΔK = stress intensity range [N/mm$^{3/2}$]

$log\ C(R)$ = intercept on the log da/dN axis.

M = slope of the da/dN versus ΔK curve

Results of the constant amplitude fatigue tests were transformed to an effective stress intensity range, ΔK_{eff}, accounting for the influence of the stress ratio and crack closure effects, using the Forman Mettu approach [Forman & Mettu, 1992] presented in Annex A:

$$da/dN = C_{eff} \cdot \Delta K_{eff}^M = C_{eff}(U(R)\Delta K)^M \tag{2}$$

where the crack opening function, U, describes the influence of R so that C_{eff} is independent of R.

Estimates of parameters $C(R)$, $U(R)$, C_{eff}, and M were obtained through linear regression of the experimental data. The mean value of $C(R)$ or C_{eff} (50% probability of survival) and the scatter band (lower bound 97.7% and upper bound 2.3% probabilities of survival) were determined. In general, the data in the first 0.25 to 0.5 mm crack extension were ignored because the crack growth rate for such a small crack extension may be influenced by crack initiation, from a blunt original notch to a sharp fatigue crack. The standard BS7910:2019 is widely used in fatigue crack growth and fracture analyses. The standard presents the crack

growth rates for stress ratio $R < 0.5$ and $R \geq 0.5$, thereby assuming a bi-linear relationship between $\mathrm{d}a/\mathrm{d}N$ and ΔK for steels, with different parameters for C and M depending on the environment (air /sea water / cathodic protection) and the stress ratio R.

In this study, the slope M of the $\mathrm{d}a/\mathrm{d}N$ versus ΔK curve is either estimated from the data over a certain range of ΔK values using Eq. (3), or fixed to a value $m = 2.88$, the latter being equal to the value of the second part of the bi-linear relation in BS7910:2019.

$$\widehat{M} = \frac{n\sum_{i=1}^{n}(\log \Delta K_i \cdot \log(\mathrm{d}a/\mathrm{d}N)_i) - \sum_{i=1}^{n}\log \Delta K_i \sum_{i=1}^{n}\log(\mathrm{d}a/\mathrm{d}N)_i}{n\sum_{i=1}^{n}(\log \Delta K_i)^2 - (\sum_{i=1}^{n}\log \Delta K_i)^2} \tag{3}$$

where:

$\widehat{M}$ = estimate of M based on the available data

n = number of data

The estimate of $\log C(R)$ or $\log C_{eff}$ is denoted as $\hat{C}$. Combining Eq. (2) and (3) and considering the arithmetical mean, $\hat{C}$ is obtained with:

$$\hat{C} = \frac{1}{n}\left(\sum_{i=1}^{n}\log(\mathrm{d}a/\mathrm{d}N)_i + \widehat{M}\sum_{i=1}^{n}\log \Delta K_i\right) \tag{4}$$

The estimate of the standard deviation in terms of the dependent variable $\mathrm{d}a/\mathrm{d}N$, s, is calculated with:

$$s = \sqrt{\frac{\sum_i\left[\log(\mathrm{d}a/\mathrm{d}N)_i - \left(\log \hat{C} + \widehat{M} \cdot \log \Delta\sigma_i\right)\right]^2}{n - x}} \tag{5}$$

where:

x = 2 if slope M is variable and 1 if slope M is fixed, considering the degrees of freedom (e.g. European Convention for Constructional Steelwork (2018)); in the latter case, M substitutes $\widehat{M}$ in Eqs. (4) and (5).

2.5 Evaluation of crack growth rate

The following sections evaluate the test data in terms of the influence on the crack growth rate of parameters material (S355G10+M, S460M), material condition (unwelded base material (BM), as welded bead-on-plate weld (BP), stress relieved bead-on-plate weld (BP), as welded K-weld (K)), and stress ratio R (0.1, 0.3, 0.5, 0.6, 0.7).

Base material specimens

The top graph of Figure 10 plots da/dN as a function of ΔK_{eff} for all base material specimens made of S355G+M (BM35-series) and S460M (BM46-series). The bottom graph of Figure 10 compares the test results at all R-ratios with the predicted crack growth rate curves according to the Forman Mettu approach (FM), using the parameters of Table A1.

Results presented as ΔK_{eff}

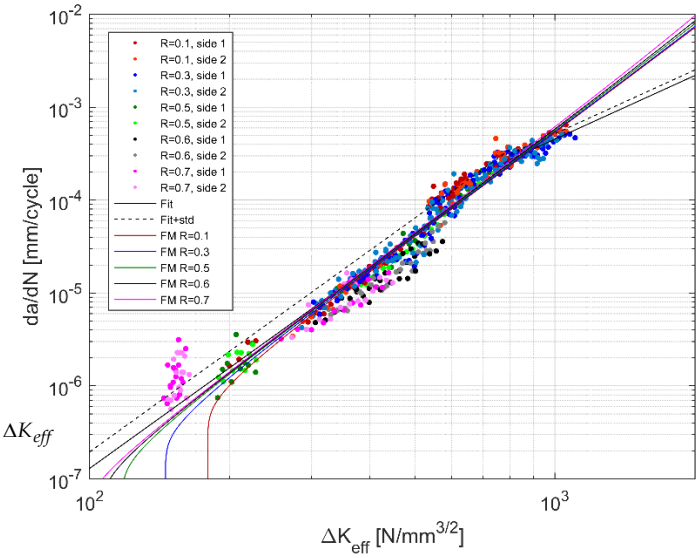

Results presented as ΔK

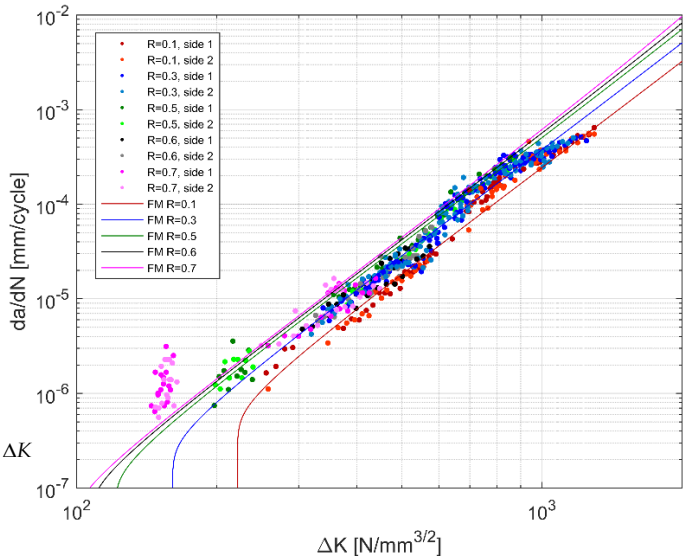

Figure 10: Experimental data (dots), mean and mean plus one standard deviation fit of those data (black curves) and Forman Mettu relation (FM, coloured curves)

With larger R value, the crack growth rate increases. Except from the data in the near threshold domain ($\Delta K < 200$ N/mm$^{3/2}$) at $R = 0.7$, there is a reasonably good match between the experimental data and the Forman Mettu approach. For $R > 0.6$, ΔK equals ΔK_{eff} using parameters in the Forman Mettu equations as given in Annex A. This assumption holds for the log-linear part of the crack growth rate curve, which is split between two log-linear relations that intersect at approximately $\Delta K = 700$ N/mm$^{3/2}$. Calibrating C_{eff} based on the Forman Mettu approach for $0.1 < R < 0.6$ gives a reasonable agreement with the test results, but the Forman Mettu approach is non-conservative if this relation is extended to $R \geq 0.7$. A consistent match could not be made for the stress ratio $R = 0.7$. It is unclear what caused the relatively fast cracking at $R = 0.7$ in the near threshold.

The steady state crack growth rate of the two tested base materials S355G10+M and S460M can be found in Figure 11, in which ΔK_{eff} is determined with $U(R)$ for similar steels according to Fitnet (2008). A more elaborative presentation of $U(R)$ is added below. The difference in growth rates between the two materials appears insignificant from this figure.

Figure 12 presents experimental data versus the crack growth rate obtained from the material parameters given in the BS7910:2019. Test results are presented as ΔK at MEAN and MEAN+2s; values according to BS7910:2019 are given for MEAN and MEAN+2s. In comparison with the test data at high ΔK (600-1200 N/mm$^{3/2}$), MEAN and MEAN + 2s values according to BS7910:2019 are non-conservative at low stress ratio ($R = 0.1$ and $R = 0.3$) and reasonably conservative for stress ratios $R = 0.5$, 0.6 and 0.7. For low ΔK values Figure 12 presents experimental data versus the crack growth rate obtained from the material parameters given in the BS7910:2019. Test results are presented as ΔK at MEAN and MEAN+2s; values according to BS7910:2019 are given for MEAN and MEAN+2s. In comparison with the test data at high ΔK (600-1200 N/mm$^{3/2}$), MEAN and MEAN + 2s values according to BS7910:2019 are non-conservative at low stress ratio ($R = 0.1$ and $R = 0.3$) and reasonably conservative for stress ratios $R = 0.5$, 0.6 and 0.7. For low ΔK values (200-600 N/mm$^{3/2}$), the MEAN results of BS7910:2019 are conservative for ratios $R \geq 0.1$.

Welded specimens

Bead-on-plate welds (single weld run) and K-welds (weld over full member thickness) were tested using base materials S355G10+M and S460 and matching filler material. Figure 13 compares the crack growth rate as a function of ΔK of the base material specimens and the bead-on-plate welded specimens for a stress ratio range of $0.1 \leq R \leq 0.7$. Here, the

external stress ratio is adopted, i.e. the ratio is not corrected for the residual stress. Considering the relatively small scatter for all combined data at various stress ratios, it appears that the crack growth rate is independent of the stress ratio for the investigated range $0.1 \leq R \leq 0.7$ for the bead on plate specimen, see the lower graph of Figure 13.

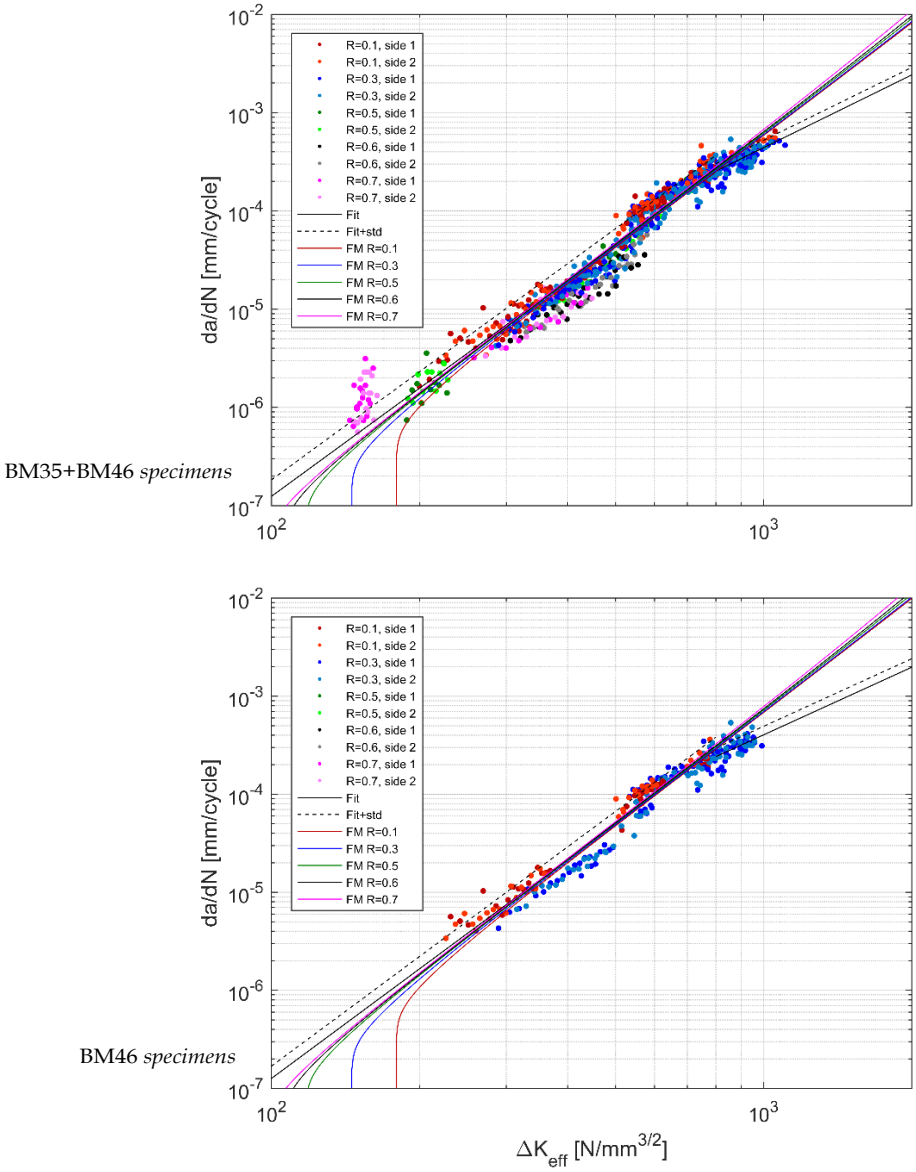

Figure 11: Experimental data (dots), mean and mean plus one standard deviation fit of those data (black curves) and Forman Mettu relation (FM, coloured curves)

A likely explanation is that the residual tensile stresses caused by welding are responsible for a fully opening crack, even at minimum stress, and even for relatively low stress ratios. It therefore seems a reasonable estimation that $\Delta K = \Delta K_{eff}$ for the bead-on-plate welded specimens. The bead on plate data match the parameters obtained for $R > 0.6$~0.7 in the base material tests, suggesting a fully opening crack at $R > 0.6$~0.7 in base material.

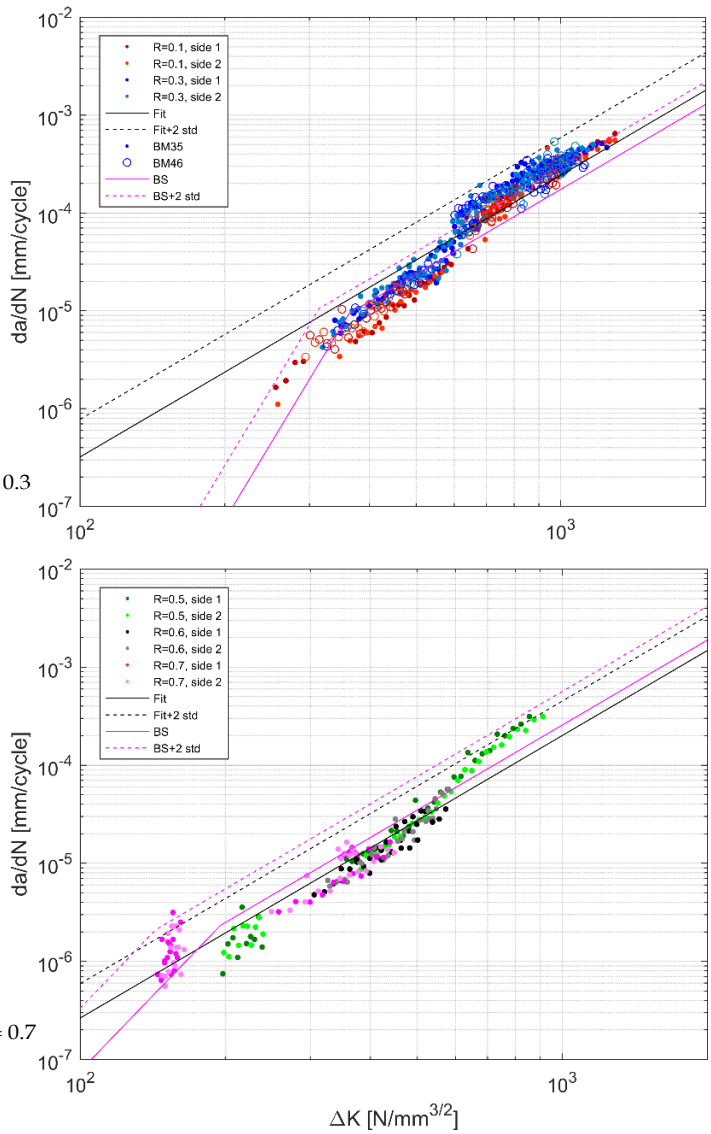

$R = 0.1$ *and* $R = 0.3$

$R = 0.5,\ R = 0.6$ *and* $R = 0.7$

Figure 12: Experimental data (dots), mean and mean plus two standard deviations fit of those data (black curves) and BS7910 mean and mean plus two standard deviations relations (pink curves)

A good agreement is observed with the material parameters presented in BS7910:2019 at high ΔK ranges (> 500 N/mm$^{3/2}$). For lower threshold levels (ΔK < 300 N/mm$^{3/2}$), the measured crack growth rate is within the scatter band of BS7910:2019. For 300 < ΔK < 500 N/mm$^{3/2}$, the BS7910:2019 gives a conservative approximation of the crack growth rate.

BM and BP results

Only BP results

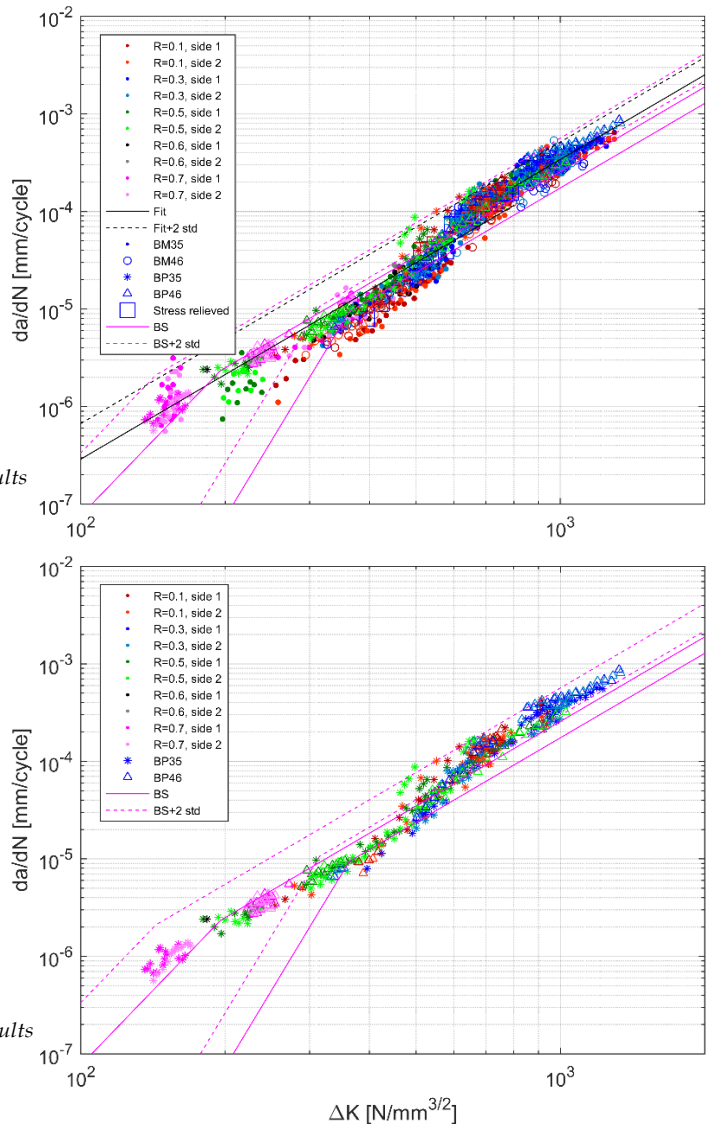

Figure 13: Experimental data (dots, with different colours for different stress ratios), mean and mean plus two standard deviations fit of those data (black curves) and BS7910 mean and mean plus two standard deviations relations at high and at low stress ratios (pink curves)

The crack growth rate of BP35 specimen series was slightly higher than the average rate of the base metal specimens, thereby showing that other factors such as grain size and homogeneity have an influence. However, the difference is small. Similar observations as given for BP35 bead-on-plate welded specimen series hold for the BP46, KW35 and KW46 specimen series results, see Figure 13 and Figure 14. All data are within the scatter band of BS7910:2019. No significant difference is found between base material and welded specimens, except from the fact that the welded specimen results tend to be more independent of the stress ratio and follow the trend of stress ratio $R = 0.7$. In other words, $U = 1$ for welded specimens and $R \geq 0.1$.

The influence of stress relieving the specimens (before testing) on the crack growth rate was studied with additional bead-on-plate specimens (BP35 series at $R = 0.1$ and $R = 0.3$). The resulting crack growth rate is given in Figure 13a. The crack growth rate is reduced through the stress relief procedure compared to the BP specimen, and it is close to the lower bound (approximately MEAN-*s*) of the BP data, predominantly at lower ΔK values, and accordingly, the lower crack sizes at which the crack growth rate was determined. This again demonstrates the influence of residual stress on crack growth rates. At higher ΔK values and hence deeper cracks, the crack growth rate of the stress relieved specimen and the non-stress relieved specimens are similar. This is explainable as the crack has then entered a zone of lower residual stresses (Figure 9), which have even reduced through shakedown.

Crack opening function

The experiments indicated that the crack growth rate of base material increases with increasing stress ratio, which is confirmed by literature findings. Alderliesten (2016) explains that a certain stress range $\Delta\sigma$ (and thus ΔK) but with a higher R, results into more cyclic work being applied and hence higher crack growth rate at high R-values as compared to low R values. The experimental results for all R values ($R = 0.1$, 0.3, 0.5, 0.6 and 0.7) were statistically evaluated to determine the estimate of U in a similar fashion as $\widehat{M}$ in Eq. (3). Because of the relatively small differences between the BM35 and BM46 series, these data points were merged. Data of welded specimens were not included in the evaluation of the U-estimate. The obtained relationship between U and R is presented in Table 5 and Figure 15 (in dots) in comparison with literature results (in lines). The data of the current paper are in the scatter band of other data, but the effect of the stress ratio on crack closure is less pronounced in the current data.

2.6 *Pivot points*

Yamada et al. (2011) and Schijve et al. (2004) present slope changes in the crack growth rate as a function of the stress intensity range for 2024-T3 bare aluminium alloy. Yamada et al. (2011) propose modified crack growth models with adjusted constraint factors for

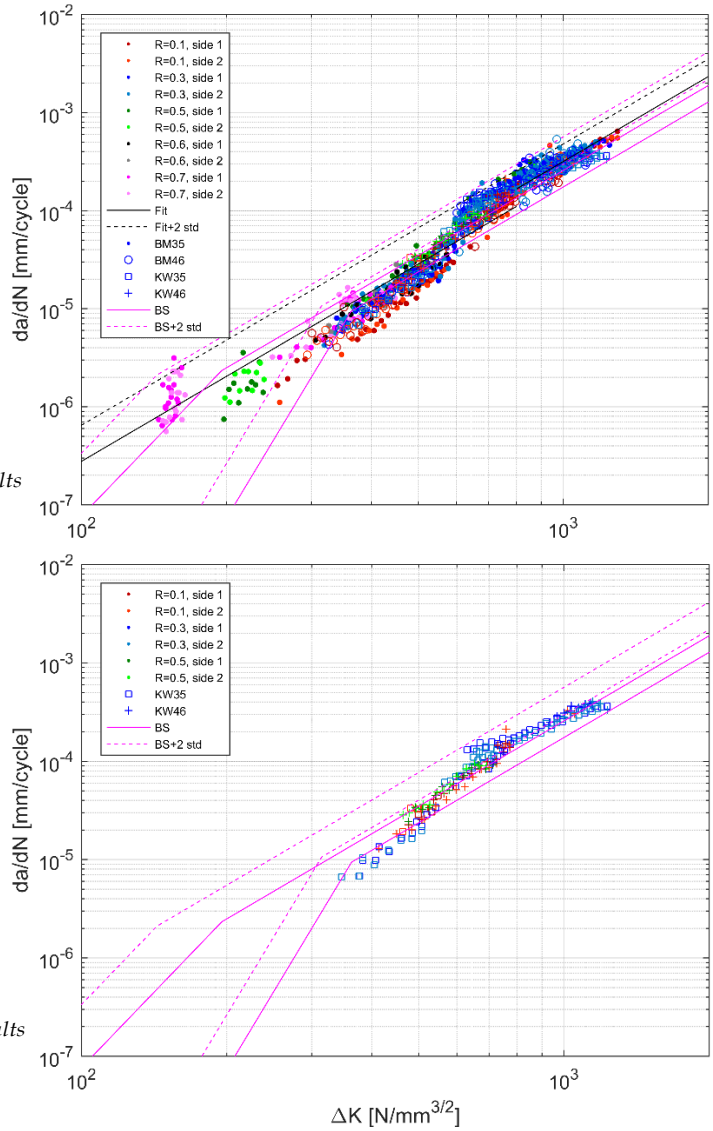

Figure 14: Experimental data (dots, with different colours for different stress ratios), mean and mean plus two standard deviations fit of those data (black curves) and BS7910 mean and mean plus two standard deviations relations at high and at low stress ratios (pink curves)

Table 5: R-ratio parameters

R	*U*
0.1	0.86
0.3	0.91
0.5	0.95
0.6	0.95
0.7	1.00

predicting the crack growth rate. Slope changes, e.g. shown in [Amsterdam and Grooteman, 2006] generally coincide with transitions in mechanisms or crack surface morphology, which might explain the crack growth behaviour in the steel specimens of the current study as well.

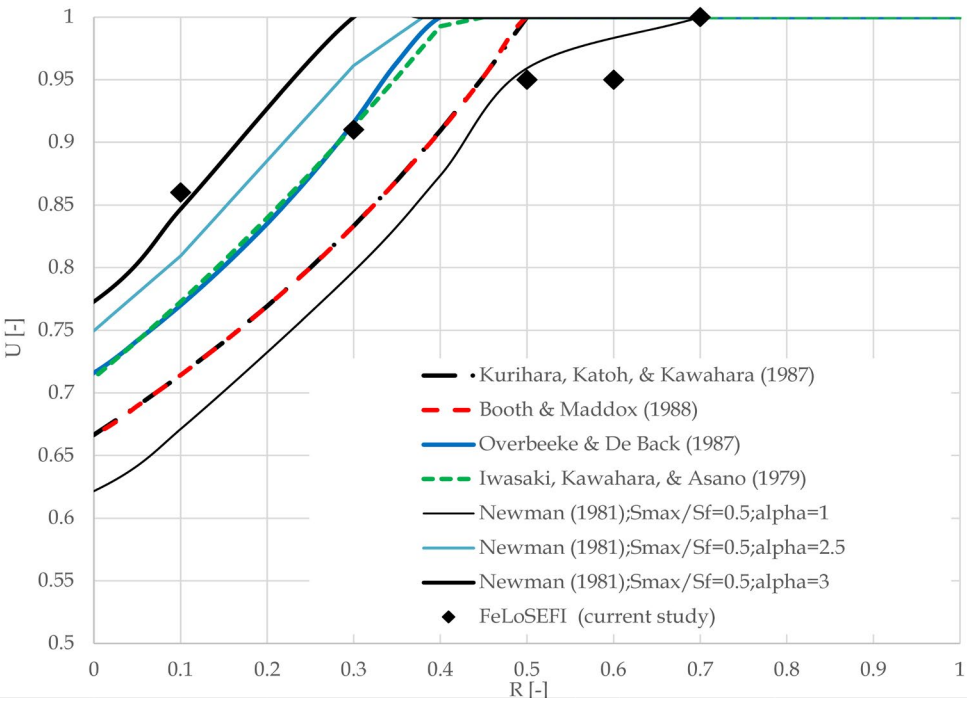

Figure 15: U as function of R based on test results against literature data of Booth & Maddox (1988), Overbeeke & De Back (1987), Newman (1981), Iwasaki, Kawahara, & Asano (1979) and Kurihara, Katoh, & Kawahara (1987)

Slope changes are also observed in the data of the specimens tested herein. A differentiation in the description of the crack growth curves into multiple zones leads to a

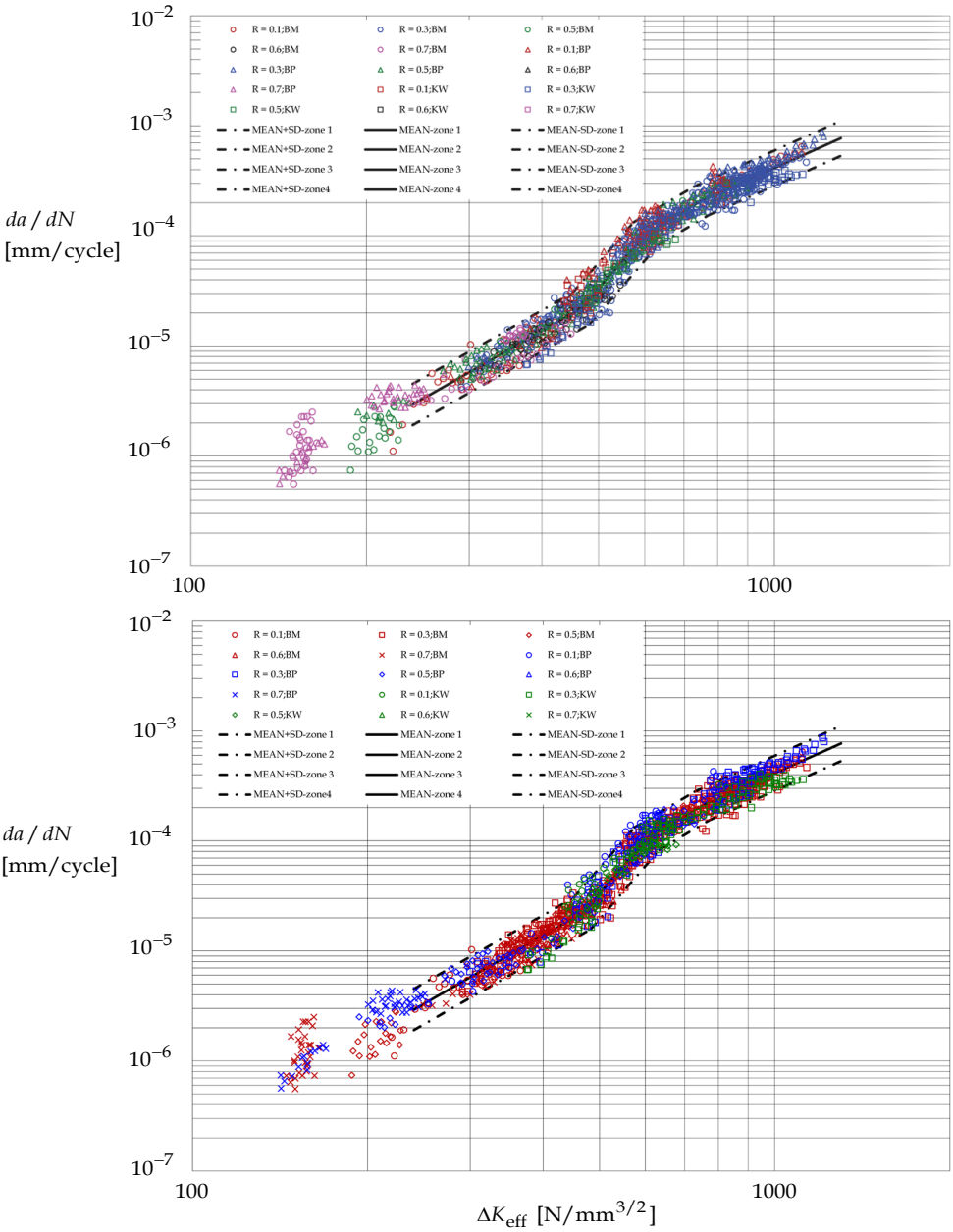

Figure 16: Experimental results of all test data 'corrected' with the newly obtained U(R) factors at minimum standard deviation

more accurate representation than the linear, or a bi-linear approximation used in section 2.4 of the current paper.

Figure 16 presents again the mean crack growth rate including scatter (mean ±s) of all coupon test series but now using the modified relationship $U(R)$ in ΔK_{eff}. In this evaluation, also the welded specimen results were included. Up to a value of $\Delta K_{eff} = 500$ N/mm$^{3/2}$, (crack length of about 7 mm), it was assumed that the tensile residual stresses were such high that the effective stress ratio was $R = 0.7$ and thereby $U = 1$. Above the $\Delta K_{eff} = 500$ N/mm$^{3/2}$, it was assumed that the effective stress ratio was according to nominal ratio.

Four zones can clearly be distinguished with different crack growth rates, excluding the near-threshold regime at approximately $\Delta K_{eff} < 250$ N/mm$^{3/2}$. Table B4 in appendix B lists the slope, crack growth constant and exponent as well as the standard deviation for each zone. Table B5 lists the positions of the pivot points per zone. The crack depths of 3, 9, 13 and 20 mm as applied in the fractographic investigation shown before, are in the four distinguished zones. (In specimen BM1035, these crack depths correspond with $\Delta K_{eff} = 350$, 591, 730 and 1050 N/mm$^{3/2}$, respectively).

Figure 17a: Fracture surfaces of three base material specimens, BM0835, BM1035 and BM1135

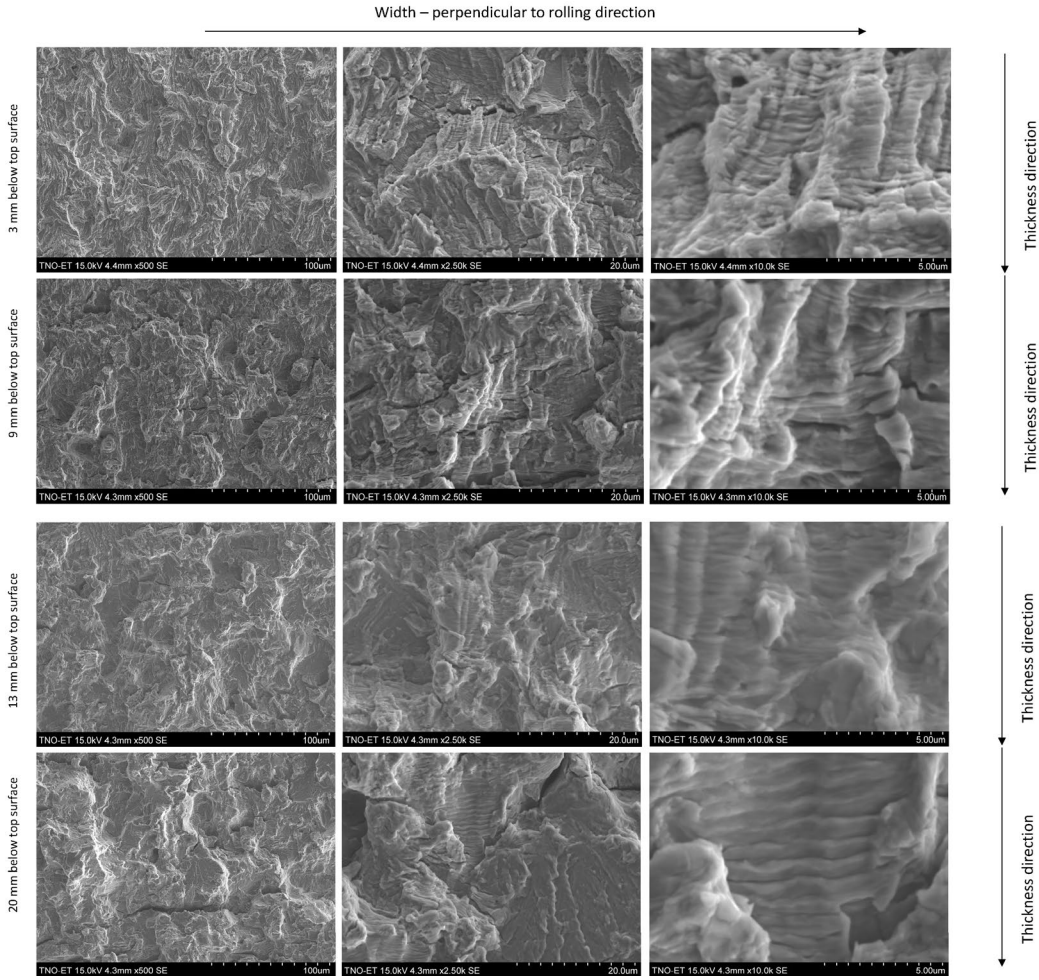

Figure 17b: Fracture surface of BM1035 at multiple crack depths

As observed from Figure 7 and Figure 17, no obvious distinction was found between these four depths on the fracture surface, except from the observation that the density of secondary cracks increased near zone 4 (crack depth up to 20 mm from the surface). This implies that more work must be done to propagate the crack. This could explain the lower flatter slope of the crack growth curve at 20 mm depth.

2.7 Evaluation of load sequence effects

Figure 18 and Figure 20 show the crack growth rate as a function of the stress intensity range in specimens BM1535 and BM1735, respectively, where the vertical black curves

indicate the application of an OL. The trends in crack growth data following the OL in these figures are representative for all test performed with OL. Qualitatively, the following observations can be made from the test results. For all materials and conditions, the experiments performed indicate that overloads increase the short-term crack growth rate directly following the overload and after a certain crack extension, the crack growth rate reduces relative to the CA crack growth rate. Similar observations are given e.g. in Lu et al. (2019) and Borrego et al. (2003). At larger crack extensions, the crack growth rate gradually increases up to the attainment of the CA rate. Changes in growth rate caused by stress peaks or throughs are further referred to as load sequence effects. In all tests it was observed that a single OL causes crack growth retardation, whereas an UL causes crack growth acceleration. These observations are in line with literature. For example, Mohanty et al. (2009) have found the effect of retardation after a single overload. Yuen & Taheri (2006) report retardation effects due to multiple overloads.

Zitounis & Irving (2007) show acceleration due to a single underload. The same is observed here, but the acceleration as a result of an UL appeared negligible compared to the retardation effect following an OL of similar magnitude. A more important influence of an underload is that it reduces the retarding effect of a preceding overload, which is in line with the findings of Bacila et al. (2007) and Rushton & Taheri (2003).

Load sequence effects are also observed in case of an applied load sequence that consists of a block of constant amplitude loading with subsequent mean shifts. The shifted maximum or minimum stress at the transition between blocks is found to act similar to an UL or OL. Sander & Richard (2006) showed that an acceleration is obtained by a low–high block loading, while a high–low sequence leads to a retardation. The effect of block loading depends on the block loading ratio and the length of the block loading.

Updated fatigue crack growth modelling in steel including the observed load sequence effects is treated in more detail by Maljaars & Tang (2019). A qualitative analysis of the observed load sequence effects is presented here. Figure 18 and Figure 20 present the crack size and loading as a function of number of cycles in specimens BM1535 and BM1735, respectively, giving an indication of the resolution of the measurements.

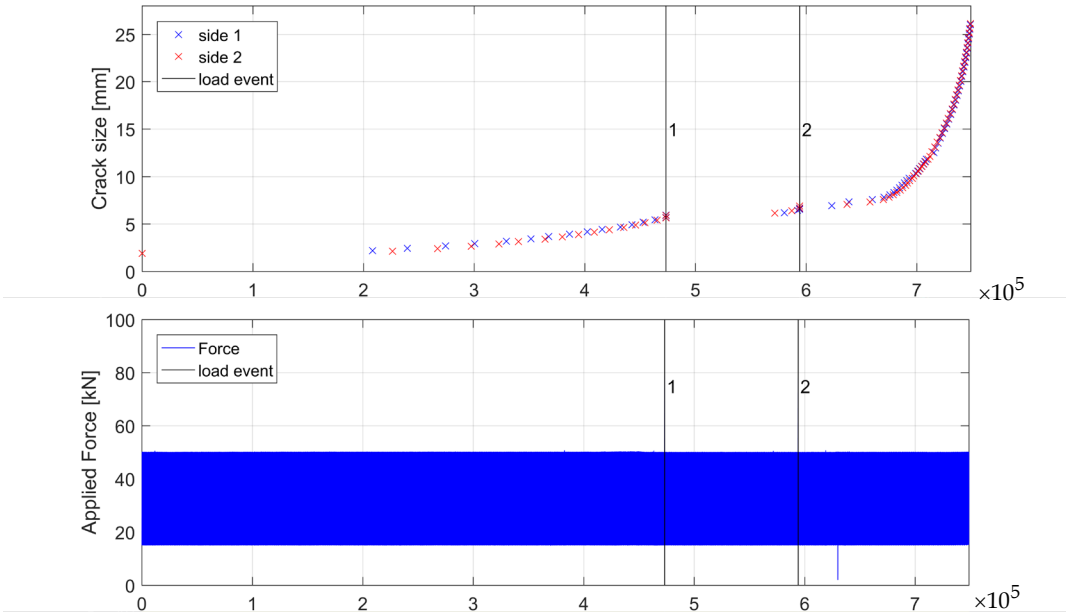

Figure 18: Crack size and loading as a function of number of cycles in specimen BM1535

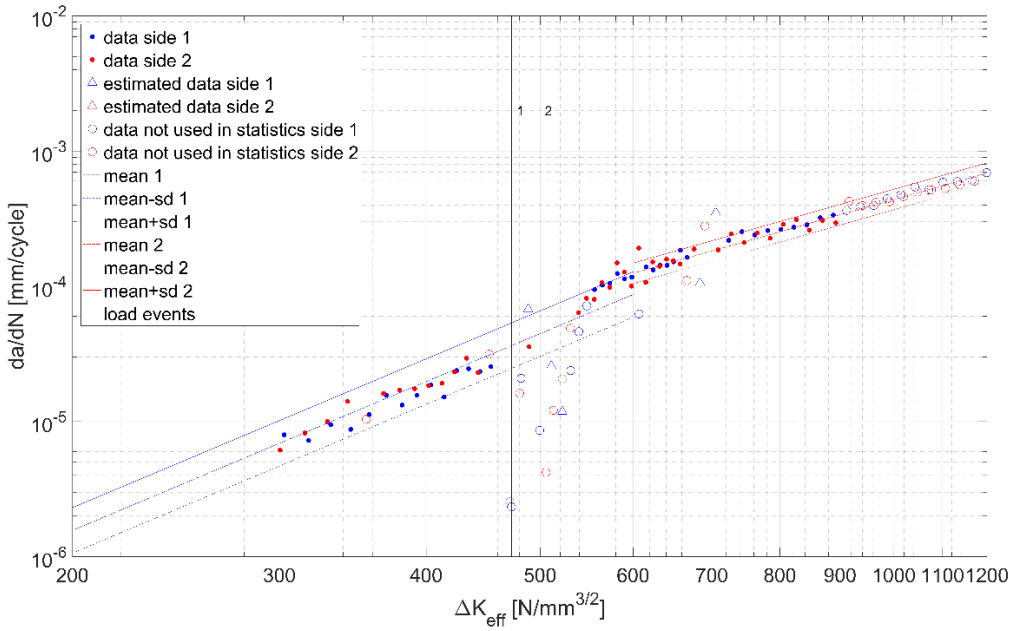

Figure 19: Crack growth rate as observed in specimen BM1535; 'estimated data': data retrieved from photo analyses; 'data not used in statistics…': data not included in deriving the mean and characteristic crack growth curves in this graph

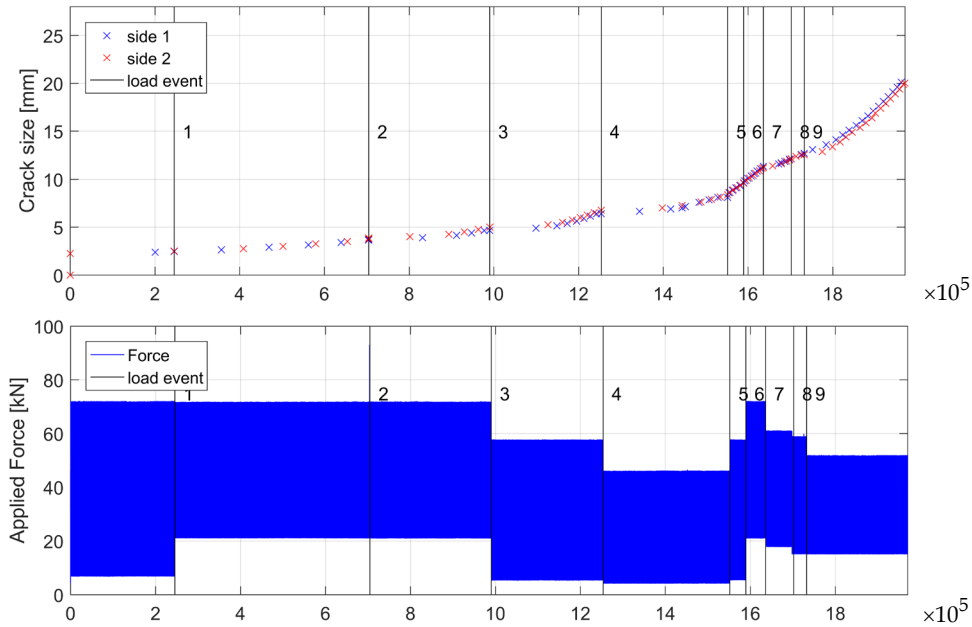

Figure 20: Crack size and loading as a function of number of cycles in specimen BM1735

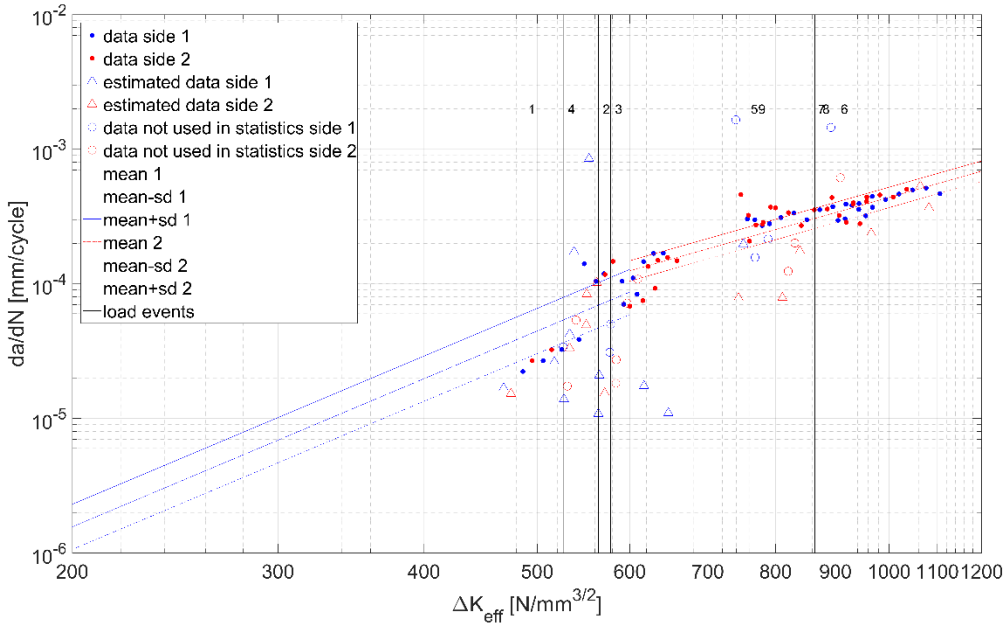

Figure 21: Crack growth rate as observed in specimen BM1735; 'estimated data': data retrieved from photo analyses; 'data not used in statistics…': data not included in deriving the mean and characteristic crack growth curves in this graph

The observed influences on the crack growth rates were quantified hereafter for the following load events: overload (OL), underload (UL) mean change down (MCD), mean change up (MCU), overload directly followed by underload (OL+UL), and mean change down followed by mean change up (MCDU). Two indicators were used to represent the magnitude relative to the CA stress ranges. The first indicator – D_{OL} or D_{UL} according to (6)– expresses the ratio of the stress range between OL or UL and CA. The stress ratio R does not influence this indicator. On the other hand, the second indicator – A_{OL} according to (7) expresses the ratio in maximum stress between OL or UL and CA.

$$D_{OL} = \frac{S_{max,OL} - S_{min}}{S_{max} - S_{min}} = \frac{\Delta S_{OL}}{\Delta S} \qquad (6)$$
$$D_{UL} = \frac{S_{max} - S_{min,UL}}{S_{max} - S_{min}} = \frac{\Delta S_{UL}}{\Delta S}$$

where,

D_{OL} = ratio of stress range between OL and CA

D_{UL} = ratio of stress range between UL and CA

$S_{max,OL}$, ΔS_{OL} = maximum stress, and stress range at overload

$S_{min,UL}$, ΔS_{UL} = minimum stress and stress range at underload

S_{max}, S_{min}, ΔS = maximum stress, minimum stress and stress range of constant amplitude load after overload.

$$A_{OL} = \frac{S_{max,OL}}{S_{max}} \qquad (7)$$

where,

A_{OL} = ratio in maximum stress between overload and CA.

To quantify the load sequence effect, the number of cycles is observed after the load event ($N = N1$) and an (arbitrarily selected) crack extension of 1 mm away from the load event ($N = N2$). The average crack growth rate for the crack extension of 1 mm is then determined subsequently as (8):

$$da/dN_{load\ sequence} = \frac{1}{N2 - N1}\left[\frac{\text{mm}}{\text{cycle}}\right] \qquad (8)$$

As crack sizes usually differed on the two sides of the specimens, the evaluations were done for available crack size data for each side individually. The effective stress intensity range ΔK_{eff} is determined based on crack depth and subsequent stress range of the CA loading following the OL,OL+UL,MCD or MCDU. For the same value of ΔK_{eff}, the constant amplitude crack growth rate da/dN_{CA_mean} is calculated with the crack growth law and material parameters given in Annex B, Table B1 (representing mean lines in Figure 11;Left). Finally, load sequence factor f_{dadN} is (9) defined as:

$$f_{dadN} = \frac{da/dN_{load\ sequence}}{da/dN_{CA\_mean}} \tag{9}$$

This load sequence factor is averaged for the measurements on both sides of the specimen. The full list of results is provided in Annex B.

Figure 22 shows the resulting crack growth rates of all test data, differentiated by four zones with various crack growth rates between the pivot points versus the load sequence effects. Figure 23 presents the resulting load sequence effects on the crack growth rate

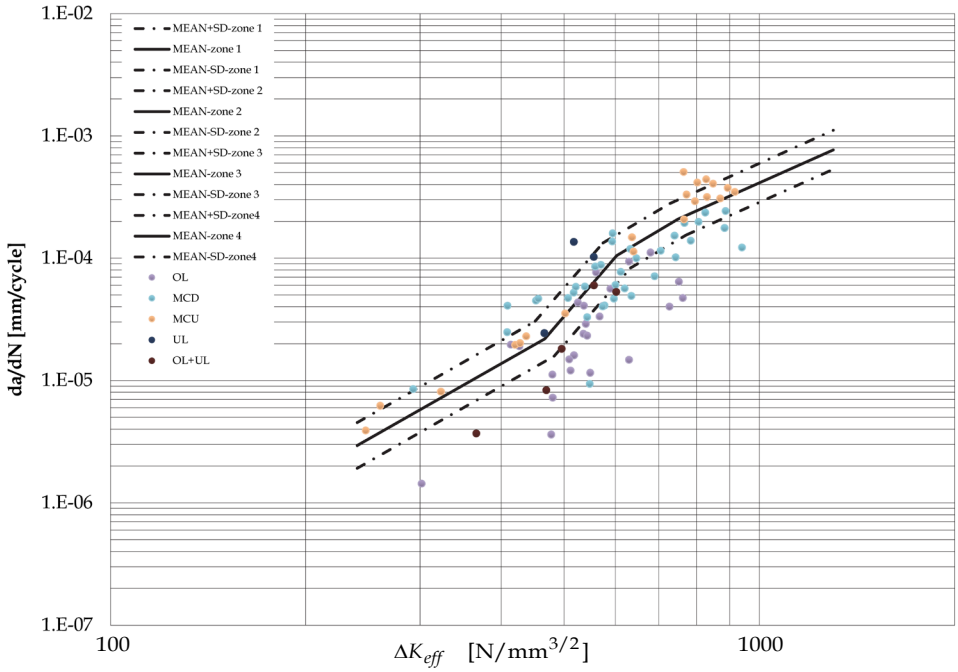

Figure 22: Resulting crack growth rates of all test data, differentiated by four zones with various crack growth rates between pivot points versus load sequence effects

based on Eq. (9). The following observations were made for OL and MCD. The average load sequence factor increases with A_{OL} and D_{OL}, although the latter relation is not strong. There is no clear difference between steel grades S355 and S460. The scatter in the load sequence factor tends to increase with A_{OL} and D_{OL}. Results of base material (BM) and

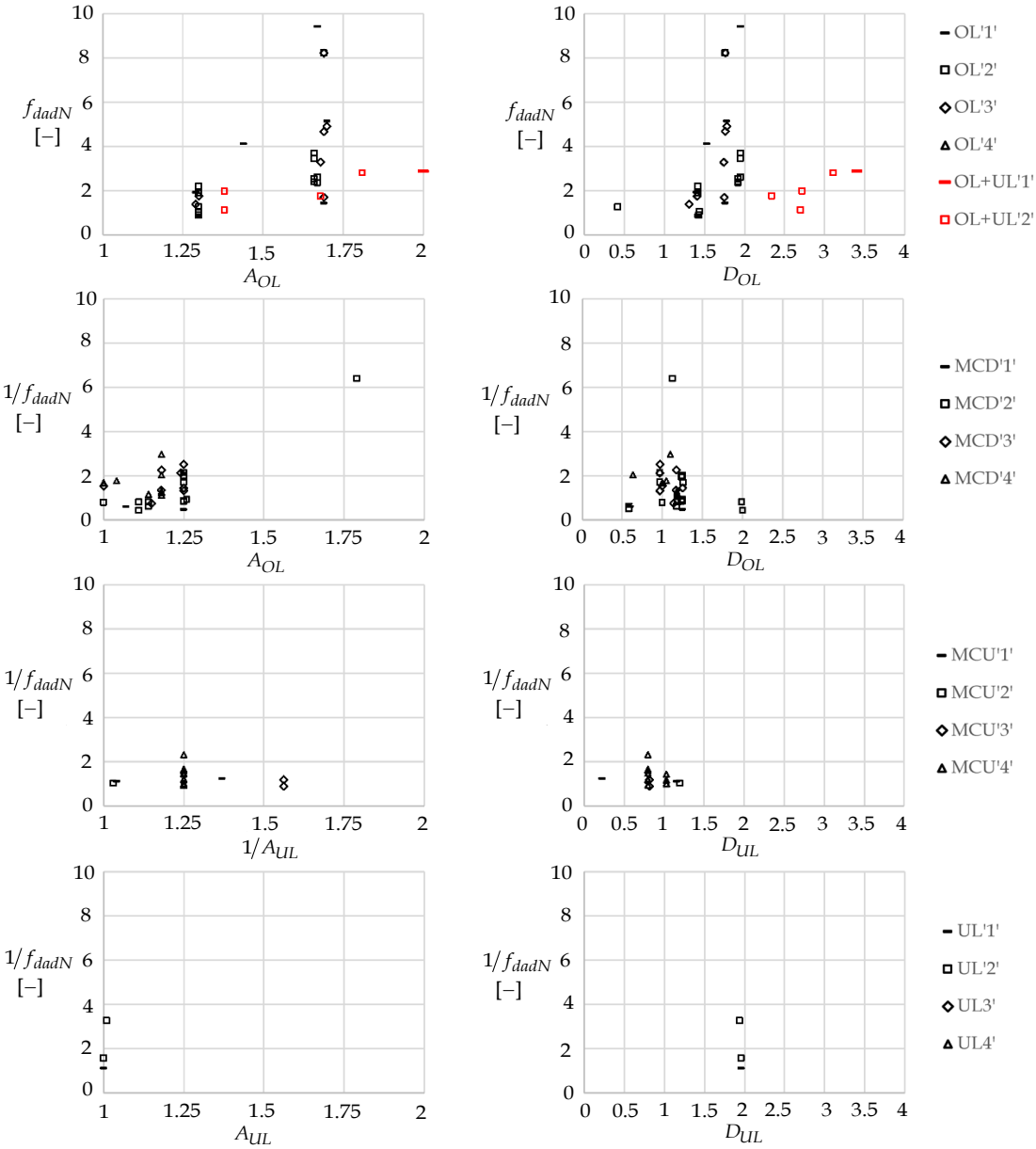

Figure 23: Load sequence effects on the crack growth rate

welded specimens (BP and KW) are similar, but both prone to large scatter. If an overload is directly followed by an underload (OL+UL) or a mean change down followed by a mean change up (MDCU), the retardation effect is reduced or even cancelled out. An underload (UL or MCU) accelerates crack growth, but this effect is less significant than the effect of an overload.

2.8 Evaluation of S-N curves

This section intends to provide background to standardisation for application in practice, in which fatigue analyses are typically carried out with the use of S-N curves. An S-N curve provides the number of fatigue cycles as a function of the stress range. The number of cycles usually covers the entire life – including initiation and propagation up to fracture – but in this paper it refers to crack growth over a certain crack extension. Table 5, Figure 23 and Figure 25 summarise the results of constant amplitude (CA) loading tests at stress range $\Delta\sigma$. The number of cycles is taken for the crack growth between 2 mm and 12 mm ($N_{2mm\text{-}12mm}$). Based on a linear regression analysis, the mean fatigue strength (50% probability of survival) and the scatter band was determined (lower bound 97.7% and upper bound 2.3% probability of survival). For this, the log-log (power law) relation between the number of cycles to failure N and the stress range was used according to (10), equivalent to the standard S-N curve, e.g. DNVGL-RP-C203 (2016):

$$\log N_{2mm\text{-}12mm} = \log b - m\,(\log \Delta\sigma) \tag{10}$$

where

$N_{2mm\text{-}12mm}$ = Number of cycles required to grow the crack from 2 mm to 12 mm depth.
$\log b$ = intercept on the log N axis
m = slope parameter of the S-N curve
$\Delta\sigma$ = stress range [MPa].

The slope parameter m of the S-N curves was either based on the result of linear regression and determined in a similar way as for M in Eq. (3), or fixed to a value m = 3.66, equal to the mean slope M of the crack growth rate as a function of the ΔK (see Table A1). The number of specimens in the linear regression analysis is n. Log a is obtained in a similar way as log C in Eq. (4). The regression line has two random unknowns log b and m, which results in a number of degrees of freedom of n - 2 using a variable slope m, that is determined in the regression analysis by the least-square method. Use of a fixed slope

reduced the number of degrees of freedom to n - 1. The standard deviation in terms of N is calculated according to (11):

$$s = \sqrt{\frac{\sum[\log N_i - (\log b - m \cdot \log \Delta\sigma_i)]^2}{n - x}} \tag{11}$$

in which x = 2 if slope m is variable and 1 if slope m is fixed. Table 6 gives the results of the regression analysis, in which all data with different stress ratios were considered as one group. Figure 24 and Figure 25 presents the results of the individual tests.

Table 6: S-N results of specimens without load sequence effects

Specimen	Specimen	$\Delta\sigma$	$N_{2mm\text{-}12mm}$	R
1	BM0935	108	699413	0.60
2	BM1035	120	548040	0.29
3	BM1135	211	84965	0.10
4	BM1335	121	655255	0.10
5	BM1835	108	787412	0.60
6	BM1935	108	567818	0.60
7	BM2035	119	506365.5	0.10
8	BM2435	121	441386	0.10
9	BM2635	85	1923775	0.69
10	BM0646	102	1350000	0.07
11	BP1235	121	385000	0.10
n		11 samples		
		Free slope	Fixed slope	
m		3.44	3.66	
s		0.096	0.093	
k		3.45	3.45	
Log b		12.87	13.32	
Log(b – ks)		12.54	13.0	
Log(b + ks)		13.2	13.6	
At $N = 10^7$:				
$\Delta\sigma_{MEAN}$ [MPa]		51.0	53.6	
$\Delta\sigma_{MEAN\text{-}2s}$ [MPa]		40.9	43.8	
$\Delta\sigma_{MEAN+2s}$ [MPa]		63.6	65.7	

At free slope parameter m = 3.44, s = 0.096 and at fixed slope parameter m = M = 3.66, s = 0.093. The slightly steeper slope of the S-N curve is attributed to the different stress ratios considered in one regression; the tests with the lowest stress ratios for which a relatively higher fatigue life is expected based on the fracture mechanics evaluation were carried out

at relatively high stress range, and vice versa. The figure also shows that test series BP35 at R = 0.1 is on the lower band of the other test data. This again demonstrates the influence of

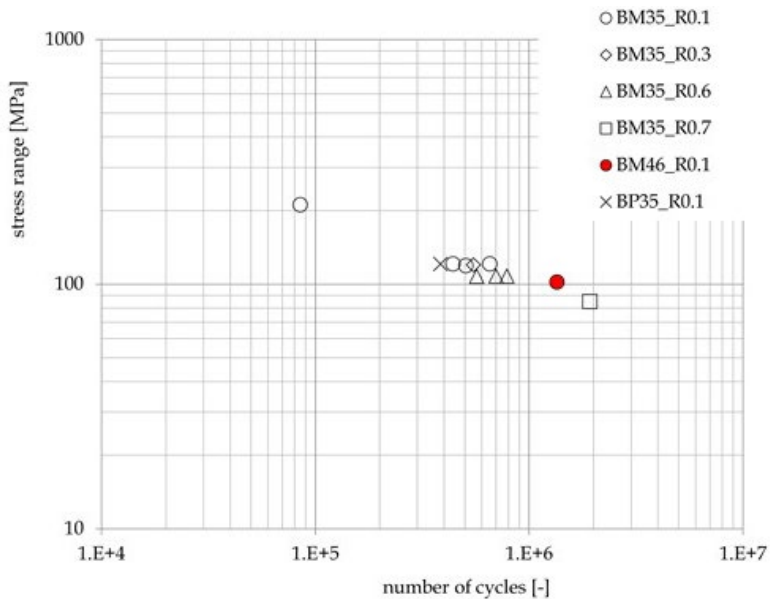

Figure 24: Results of crack growth tests at CA in S-N curves

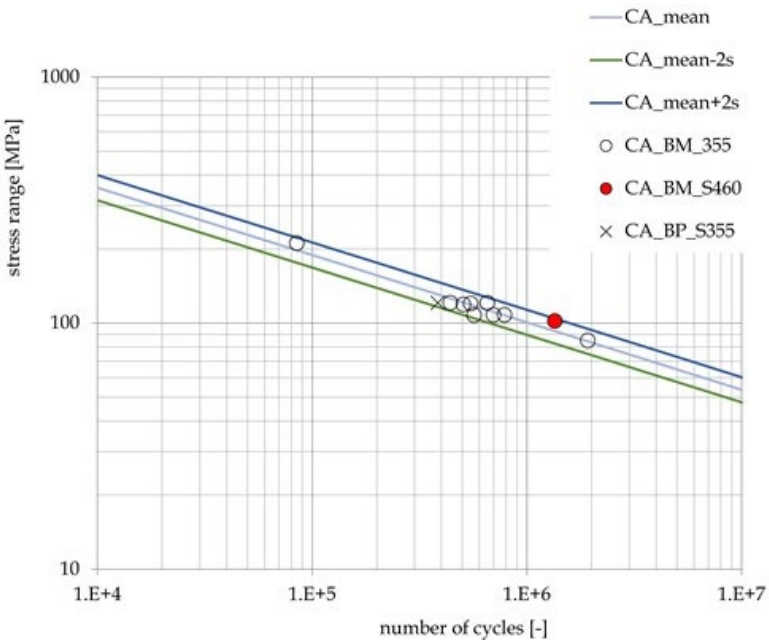

Figure 25: Results of crack growth tests at CA in S-N curves, using m=3.66

the stress ratio, since higher residual stress are expected in this specimen. Test BM46 with higher steel grade is on the higher band of the other test data. This was not expected, as the crack growth rate in high-strength materials is generally higher as compared to low-strength materials, e.g. ref. De Jesus et al. (2012). However, the different conditions in the tests apparently have just a small influence, considering the similar free and fixed slope parameters and the small scatter, which is similar to the scatter of tests carried out in a single condition (see the BM35 series at R = 0.6).

Typically, the standard deviation on log b in fatigue analyses of welded connections s = 0.2 [DNVGL-RP-C203, 2016]. The difference with the smaller standard deviation found herein is attributed to the larger scatter in crack initiation and surface notch effects and both effects are not present in the current evaluation of growth between 2 and 12 mm deep cracks. The standard deviation of the crack growth rate analysis that resulted in M = 3.66 is 0.17 with inclusion of all BM35 and BM46 series results, which is slightly higher than the standard deviation on log b. This difference is attributed to small, temporary crack arrest and acceleration effects during crack growth, related to microstructural variations (e.g. grain boundaries). These effects are visible in the crack growth rate analysis but (partially) compensate each-others influence when considering crack extension over a larger size as in the S-N curve.

The load sequence effects were also evaluated using S-N curves for a crack extension from 2 mm until 12 mm depth. As the load histories contain variable amplitudes, an equivalent stress is determined through Eq. (12), modified from Hobbacher (2016).

$$\Delta\sigma_{eq} = \left[\frac{\sum_{i=1}^{k} n_i \cdot {\Delta\sigma_i}^m}{\sum_{i=1}^{k} n_i}\right]^{1/m} \tag{12}$$

where k is the number of stress blocks with variable amplitude and $\Delta\sigma_{eq}$ is the equivalent stress range that, given the S-N curve of Eq. (10), would result in the same fatigue damage as the actual load history at the same number of cycles. This equation does not consider load sequence effects. The evaluation is carried out using m = 3.66. Table 7 and Figure 26 (top graph) present the S-N curves of specimens with load sequence effects (OL, MCD, OL+UL, MCDU) and the MEAN and scatter band of the CA tests. The load sequence effects were previously described using a 1 mm crack extension after the sequence. Any

Table 7: S-N results of specimens with load sequence effects (OL, MCD, OL+UL, MCDU)

Specimen	Specimen	$\Delta\sigma_{eq}$	$N_{2mm\text{-}12mm}$
12	BM0135	197	285987
13	BM0835	62	7344229
14	BM1235	97	1714493
15	BM1535	117	710000
16	BM1735	177	173291
17	BM2135	118	545000
18	BM2535	117	700000
19	BM0146	118	692000
20	BM0246	173	177602
21	BM0346	175	187710
22	BP0235	178	149136
23	BP0435	250	79927
24	BP0535	101	423500
25	BP0635	52	9111539
26	BP0735	169	194645
27	BP0146	75	2728066
28	BP0246	169	122300
29	KW0135	155	174270
30	KW0335	120	635000
31	KW0435	123	549806
32	KW0146	131	328000
33	KW0246	186	98530

load sequence effect is activated only for a short crack extension, because of the crack closure effect. Considering a crack extension from 2 mm until 12 mm with a relatively small number (between 2 and 9) of load sequences, the effect on the total number of cycles is marginally affected by the load sequences. Most of the results therefore are within the scatter of the S-N curve based on constant amplitude loading, as given in Figure 26. However, the scatter is undoubtedly larger as compared to the CA tests.

Table 8 and Figure 26 (bottom graph) present the S-N curves of specimens with variable amplitude random loading (VAR) based on the load history of Figure 2 and the MEAN and scatter band of the CA tests. The results are within the scatter of the S-N curve based on constant amplitude loading, i.e. there is no significant effect of the applied load history on the fatigue life. This observation is based on a limited number of tests, but similar results are obtained by others, e.g. Maljaars et al. (2019). An explanation for this is that overload effects are cancelled out by quickly following underloads, as demonstrated in Maljaars & Tang, (2019) such follow-ups occur continuously in VAR. Richard & Sander

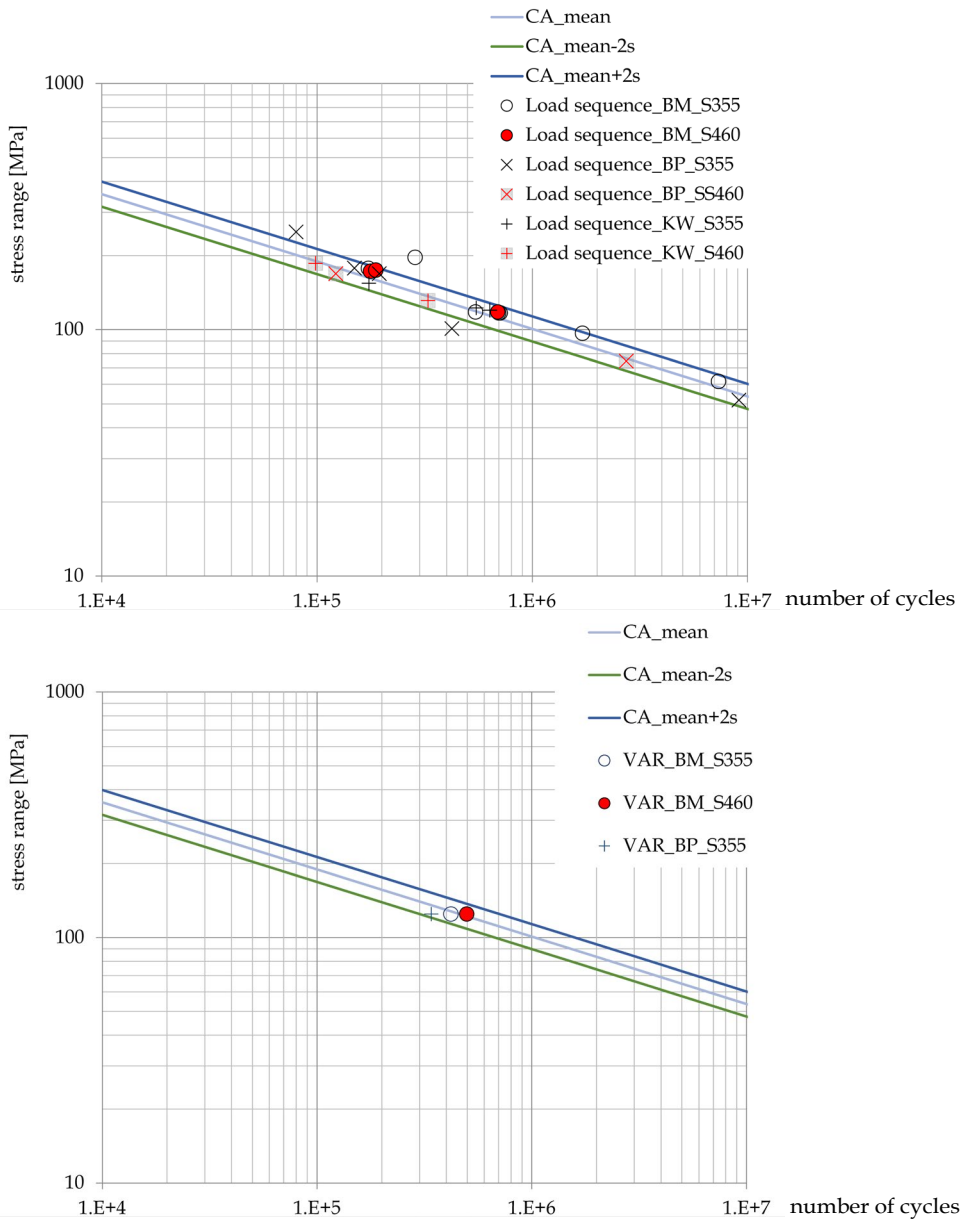

Figure 26: Results of crack growth tests in S-N curves of specimens with load sequences and variable amplitude random loading, using m = 3.66

(2006) investigated load spectra, reconstructed from rainflow method cycle counting as well as the level crossing cycle counting. Despite varying configurations of the load sequences, also in their work the spectra counted and reconstructed with the rainflow

method led to insignificant differences regarding the lifetime in comparison with the original load sequence.

Table 8: S-N results of specimens with variable amplitude random loading (VAR)

Specimen	Specimen	$\Delta\sigma_{eq}$	$N_{2mm\text{-}12mm}$
34	BM1435	125	420000
35	BM0546	125	497000
36	BP0935	125	340000

3 Tubular joint element experiments

3.1 Experimental program

To make the step towards a realistic welded joint of an offshore wind turbine foundation, a test program was set up comprising fatigue tests on almost real-scale (~50% to scale) tubular joint elements, representative of offshore wind jacket structures. The type of joint considered is a tubular joint element, See Figure 27. Retardation/acceleration of crack growth may in practice be influenced by parameters such as the residual stresses as a result of welding, load shedding and local geometry. Therefore, load sequence effects may be different in small-scale coupons as compared to these realistic tubular joint element geometry.

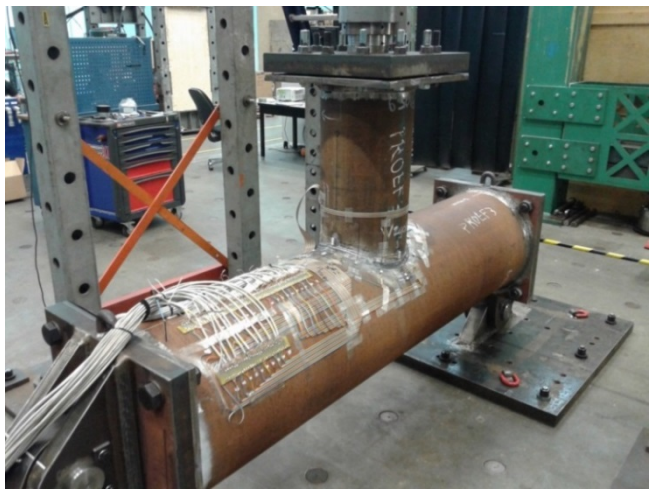

Figure 27: T-joint element

3.2 *Test rig, specimens and instrumentation*

The tubular joint elements were tested in a dedicated frame with an 800 kN servo hydraulic actuator able to apply an axial loading to the brace of the tubular joint element, see Figure 27. A tensile load is applied on the brace (vertical tube in the figure) while the ends of the chord (horizontal tube) were supported by a hinge and a roll. Table 9 presents the geometric parameters of the test specimens, See Figure 28 for explanation of symbols.

Table 9: Specimen geometric parameters

Chord			Brace					Chord	Brace	
d_0	t_0	L	d_1	t_1	θ	a	β	$2\gamma_0$	$2\gamma_1$	τ
[mm]	[mm]	[mm]	[mm]	[mm]	[°]	[-]	[-]	[-]	[-]	[-]
508	25	2000	323.9	16	90	7.87	0.64	20.32	20.24	0.64

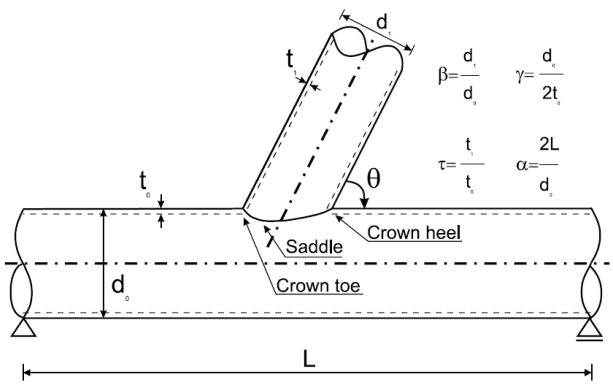

$$\gamma_0 = \frac{d_0}{2 \cdot t_0}$$

$$\gamma_1 = \frac{d_1}{2 \cdot t_1}$$

Figure 28: Parameters for tubular joint elements, given in CIDECT design recommendations [Zhao et al., 2001]

Loading

In addition to constant amplitude (CA) loading, single overloads (OL) and overloads followed by underload (OL+UL) were applied. A set of subsequent constant amplitude load blocks (VASB) was applied (representing a variable amplitude loading with mean shifts), as well as a fully variable amplitude random load (VAR) that is similar to the ones presented in Section 2.1. Table 10 summarises the loading on the tubular joint elements.

Table 10: Loading on tubular joint elements

Tubular joint element	Loading
1	CA+OL+CA
2	CA
3	VAR
4	VASB
5	VASB
6	VASB

Materials

The material of the tubular joint element and the coupon specimens (S355) have corresponding properties, but the thickness of the coupon specimens deviates from the thickness of the tubular joints for practical reasons. Crack growth in the tubular joint elements is predominantly governed by plane strain behaviour. The following materials were provided for the tubular joint elements by Salzgitter Mannesmann: 323.9 x 16 mm; EN 10210-1; S355J2H (Brace); 508 x 25 mm; EN 10225; S355G13+N (Chord). Table 11 and Table 12 list the chemical composition and the mechanical properties, respectively.

Table 11: Chemical composition (weight %)

	C	Si	Mn	P	S	Al	Cu	
S355J2H	0.15	0.19	1.39	0.01	0.001	0.035	0.02	
S355G13+N	0.15	0.27	1.44	0.011	0.003	0.043	0.02	
	Cr	Ni	Mo	V	Ti	Nb	N	B
S355J2H	0.02	0.03	0.003	0.002	0.002	0.029	0.004	0.0001
S355G13+N	0.03	0.04	0.01	0.004	0.15	0.031	0.004	0.0002

Table 12: Mechanical properties

	Ultimate strength	Yield strength	Failure strain	Charpy Toughness	Charpy test temperature
	S_u (MPa)	S_y (MPa)	A_5 (%)	Cv	T [°C]
S355J2H	518	420	36.3	198-261	-20
S355G13+N/S355J2H	514	384	34.1	163-181	-20

Instrumentation

The crack depth and length were monitored in the fatigue tests by using a number of visual and non-visual methods: strain gauges, visual observations using handheld microscopic camera Dino Lite type AM-413T with magnification of 50-200x, phased array (PA), and alternate current potential drop (ACPD). ACPD, Figure 29 and Figure 30, relies

upon the passage of a constant current through a specimen and the subsequent measurement of the electrical potential difference measured between the crack faces. ACPD is applied using (ca. 1 amp) alternating currents through the specimen using a manual tool (ACPD U8 Crack Micro Gauge). The ACPD measurements were calibrated by using calibration blocks with machined flaws. The measured crack size by ACPD was further verified by visual inspection as well as phased array measurements at the end of testing tubular joint element 1, tubular joint element 2 and tubular joint element 3, FigureFigure 30, and appeared to be ± 1 mm accurate in providing the crack depth. Strain gauges (type FLA-3-11), Figure 29, were applied around the joint; in the saddle (See Figure 28 and Figure 29). A special type of chain strain gauges is used (type FXV-1-11) to identify local stresses and local stiffness change for identifying crack activity.

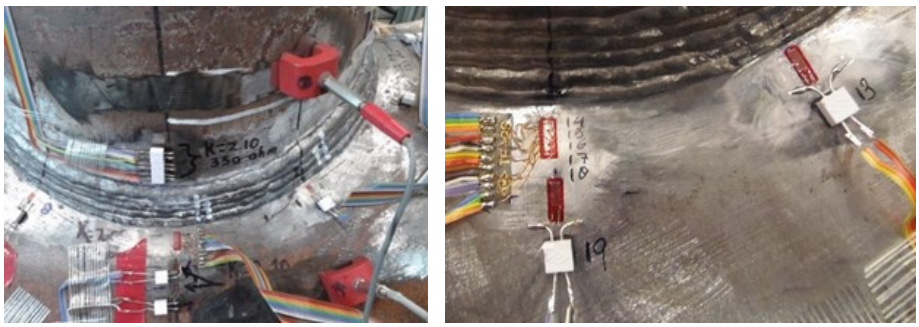

Figure 29: Left: Strain gauges and Manual ACPD current; Right: strain gauges

Figure 30: Automated ACPD, reference spacing 15 mm, 1 Amp current

Figure 31: Validation by phased array

3.3 ***Hot spot stress determination***

The chain strain gauges are measuring strain perpendicular to the weld at a distance of 4, 6, 8, 10 and 12 mm from the weld toe with a measurement length of 1 mm per position. Typically, the singularity at the weld toe causes high stress peaks near the weld toe. Crack initiation is expected at the weld toe of the crown and saddle points (See Figure 32), further referred to as the hot spot stress locations. The value of hot spot or structural stress on the surface at the hot spot is obtained by extrapolation of the stress to a potential crack initiation point. The measured strain values were linearly extrapolated to the weld toe.

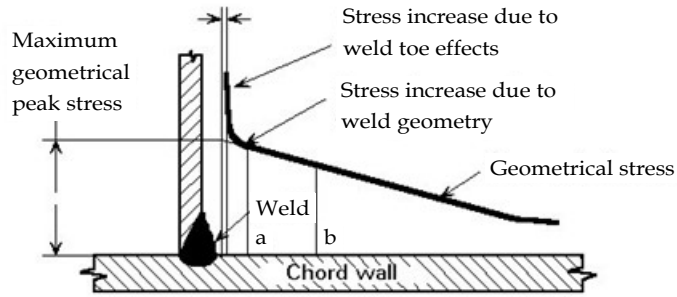

Figure 32: Locations for extrapolation of stress along the chord surface normal to the weld toe; example of stress values and extrapolation at crown

A finite element (FE) model composed of solid elements type SOLID186 was made in software Ansys version 2016 to assess local stresses and the fraction of bending in it. Figure 33 shows the principle stress direction in the vicinity of the weld and at a certain distance away from the weld in the saddle as a result of brace loading. Figure 34a presents the stress

perpendicular to the weld toe along the chord surface in the saddle position, which is the governing stress location. The hot spot stress ranges are prone to variation and randomly differ at both sides of the tubular joint element, due to local geometrical imperfections. Figure 34b provides the variation of the SCF in the chord along the perimeter of the brace, in which 0° and 180° are crown positions and 90° and 270° are saddle positions, see also Figure 33a. The stress ranges measured at the individual tubular joint elements vary due to the sensitivity to the local geometry. For evaluating the ratio of bending, the stress was linearised over the chord wall thickness in this hot spot, which is shown in Figure 34b. In agreement with DNVGL-RP-C203:2016, the hot spot stress in the weld toe is calculated based on stress linearisation, as the sum of bending and the membrane stress components. This leads to a hot spot stress of 162 MPa (at 0 mm from weld toe) and it comprises of 78% bending and 22% membrane stress.

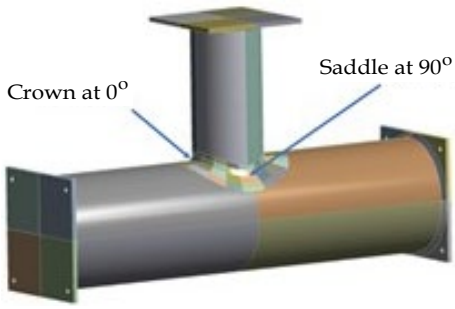

Figure 33a: Ansys FE model, with location angle around perimeter of crown and saddle

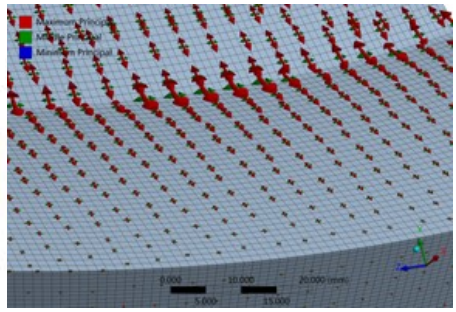

Figure 33b: Principle stress direction in the saddle as a result of brace loading

Alternatively to the FE analyses, hot spot stresses were derived by linear extrapolation of the strain gauge measurements along the chord surface to the weld toe, which were attached at a distance of 11 mm and 25 mm. The stress concentration factor (SCF) is defined as the ratio between hot spot stress and far-field or nominal stress. Figure 35 shows the stresses based on experiments and FEM as well as the SCF according to [DNVGL-RP-C203:2016], the latter based on values of [Efthymiou, 1988]. The average SCF of the tests for the current configuration is 5.56; which yields a hot spot stress range 181 MPa at 504 kN load range on the brace with a nominal stress of 32.6 MPa (brace cross sectional area A_{brace} = 15,446 mm²). Figure 36 summarises the stresses based on strain gauge measurements and the corresponding extrapolations to the weld toe. Table 13 summarises hot spot stresses based on the measurements and the corresponding numerical values of the SCF. The

average hot spot stress $\Delta\sigma_{hs}$ = 157 MPa (just below the linearised stress at 0 mm see FigureFigure 34b). The SCF according to Efthymiou (1988) is just below the maximum SCF obtained by the measurements.

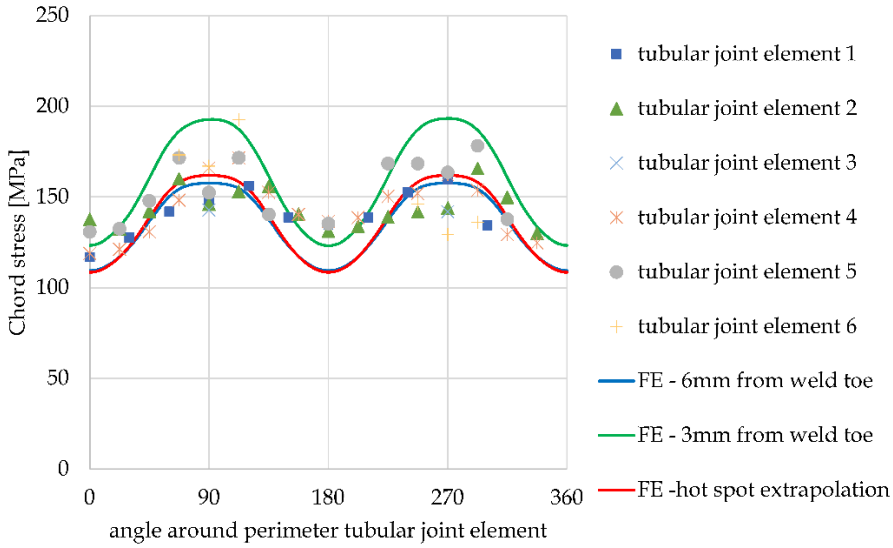

Figure 34a: Stress evaluation at 504 kN brace loading. FE model results versus measurements at 5 mm from weld toe (0° and 180° are crown positions; 90° and 270° are saddle positions)

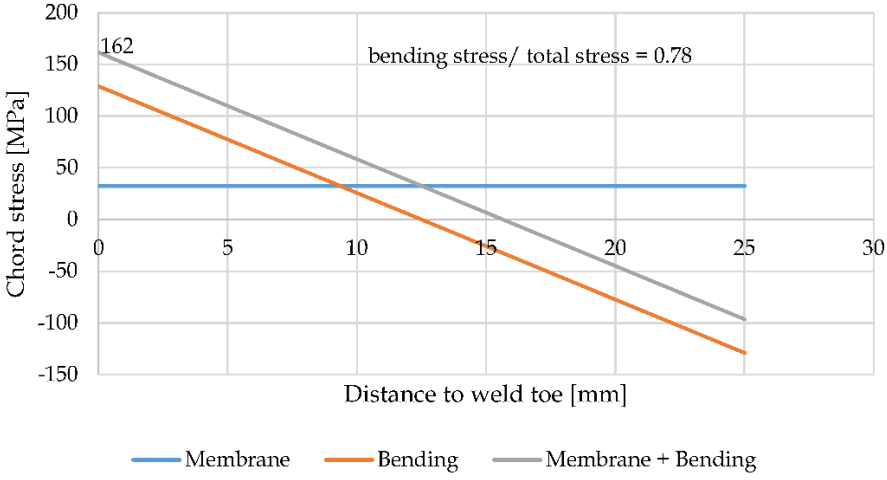

Figure 34b: Stress evaluation at 504 kN brace loading. FE model linearisation results

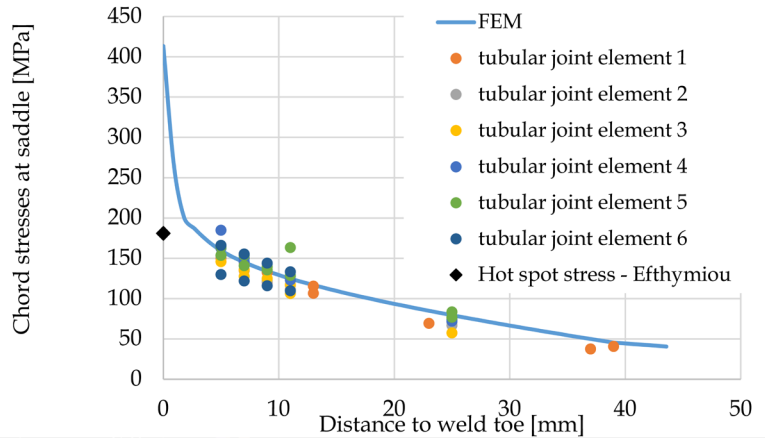

Figure 35: Comparison of linear elastic stresses at 504 kN force range based on measurements, FEM and SCF according to Efthymiou (1988)

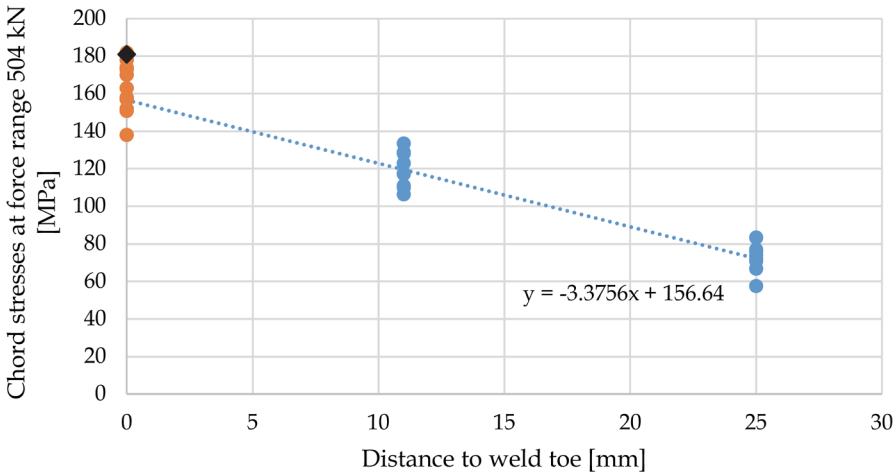

Figure 36: Comparison of stresses at 504 kN force range based on measurements at 11 mm and 25 mm including extrapolated values to 0 mm from chord weld toe and SCF according to Efthymiou (1988)

Results presented hereafter are compared against the hot spot stress according to the experiments. Note from Figure 35 that the actual peak stress in the vicinity of the weld toe, where the crack initiates, is much larger than the hot spot stress. Plasticity is therefore expected near the location of crack initiation.

Table 13: Experimental hot spot stress test results tubular joint elements

tubular joint element	Location angle [°]	Side	$\Delta\sigma_{hs;exp}$ at 504 kN	SCF_{exp}
1	240	1	170	5.21
2	270	1	157	4.81
3	270	1	151	4.63
4	270	1	173	5.30
5	293	1	174	5.33
6	293	1	138	4.23
1	90	2	157	4.81
2	68	2	158	4.84
3	67.5-90	2	152	4.66
4	68	2	182	5.58
5	68	2	163	5.00
6	90	2	178	5.46

*3.4 **Crack growth results***

The tubular joint elements were regularly inspected for determining crack size as a function of number of cycles. Typically, in the tubular joint elements, crack initiation took place at various locations close to the two saddle positions and these small cracks at each saddle position coalesced to form one dominant crack during fatigue loading. The crack sizes varied near both saddle positions of the tubular joint elements. Figure 37 gives an example of the measured crack depth as a function of the angle around perimeter (90° and 270° are saddle points) at different number of cycles, for tubular joint element 1, with an overload applied at N = 578,000 cycles.

At three characteristic stages during the fatigue test, the number of cycles was determined: 1) $N_{5\%}$ = 5% deviation of measured strain range; 2) N_{fvc} = first visual crack; 3) $N_{0.5t}$ = N at crack depth 12.5 mm. All tests were stopped before the crack grew through the chord wall thickness. Based on the available crack size information as a function of the number of cycles, extrapolations were made to determine the number of cycles at crack size at 50% ($N_{0.5t}$; a = 12.5 mm) and 100% (N_{tt}; a = 25 mm) of the wall thickness assuming constant amplitude loading without load sequence effects. Table 14 summarizes the type of loading, equivalent stress range, governing crack location and number of cycles to failure at the stages defined as $N_{5\%}$, N_{fvc}, $N_{0.5t}$ and N_{tt}. In all cases, the CA load was F_{max} – F_{min} = 560 kN – 56 kN.

3.5 Evaluation of load sequence effects

Figure 38 shows measured crack depth just before and after an OL (A_{OL}= 1.3) in tubular joint element 1, from which a retardation effect is clearly visible. The stress intensity factor at the deepest point of the cracks in the tubular joint elements was estimated using the measured hot spot stress together with the parametric equations of the stress intensity factor of a semi-elliptical crack according to Newman & Raju (1986), combined with that of simple welded joints according to Maddox and Andrews (1990),

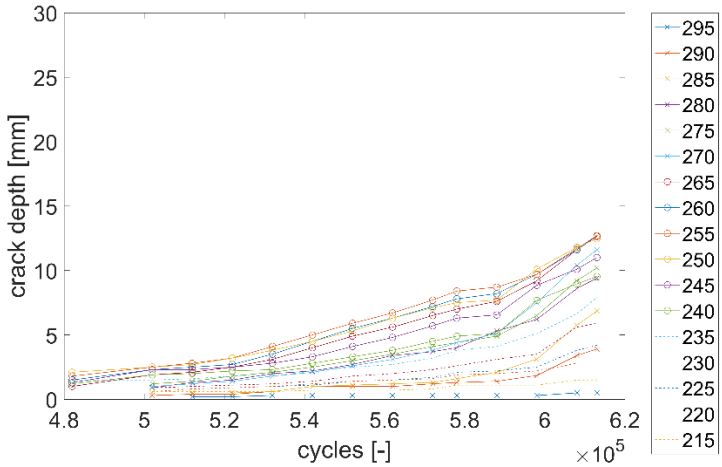

Crack depth as a function of the number of cycles at various angles [degrees] around perimeter (in legend, with 270°at saddle position)

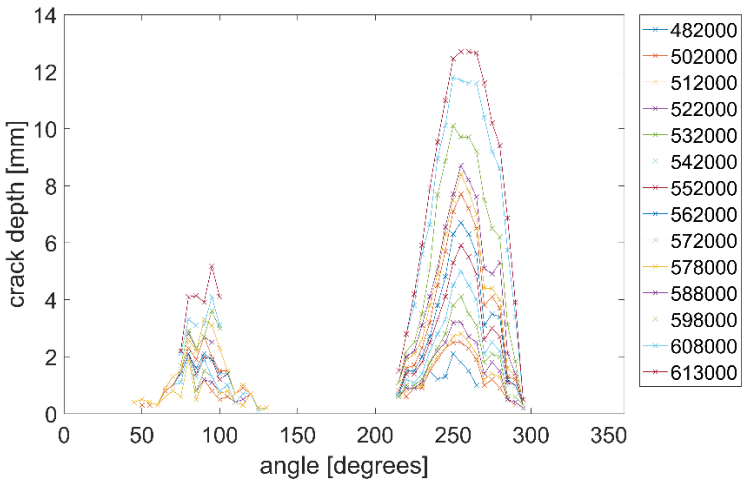

Crack depth as function of angle around perimeter at various number of cycles (legend)

Figure 37: Crack depth in tubular joint element 1 determined with APCD

Table 14: Test results tubular joint elements

Tubular joint	Loading	Side	$\Delta\sigma_{hs}$[1]	$N_{5\%}$	N_{fvc}	Locatio	$N_{0.5t}$[2]	N_{tt}[2]
			[MP	[Cycles	[Cycles	[°]	[Cycle	[Cycles]
1	CA+OL[3]+CA	1	170	450000*	482000	240	603774	653193
2	CA	1	157	517146	188000	270	788238	905259
3	VAR	1	110	600000	783761	270	107984	1179541
4	VASB	1	149	850000	608930	270	934349	1122981
5	VASB	1	150	159807	249000	293	770031	828509
6	VASB	1	150	642552	-	293	642552	
1	CA+OL[3]+CA	2	157	444201	502000	90	644853	679357
2	CA	2	158	375094	288000	68	905363	969471
3	VAR	2	111	300000	783761	67.5-90	101611	1186788
4	VASB	2	157	390684	608930	68	725912	785437
5	VASB	2	141	97922	249000	68	760041	790506
6	VASB	2	154	396439	662876	90	608782	915478

[1] equivalent hot spot stress range
[2] based on extrapolation or
[3] OL = 736 kN: N = 578000-

assuming weld attachment length $L = 0.5T$. This procedure is incorporated in BS 7910:2019 and the crack shapes in Figure 37 justify the choice of a semi-elliptical crack. Figure 39 compares the crack growth rate of the tubular joint elements with the coupon test data on KW at $R = 0.1$ and the crack growth rates according to BS7910:2019. The crack growth rate in the tubular joint elements is based on the crack depth measured by APCD up to 12.5 mm. In most cases, the number of crack sizes included in the calculation of the crack

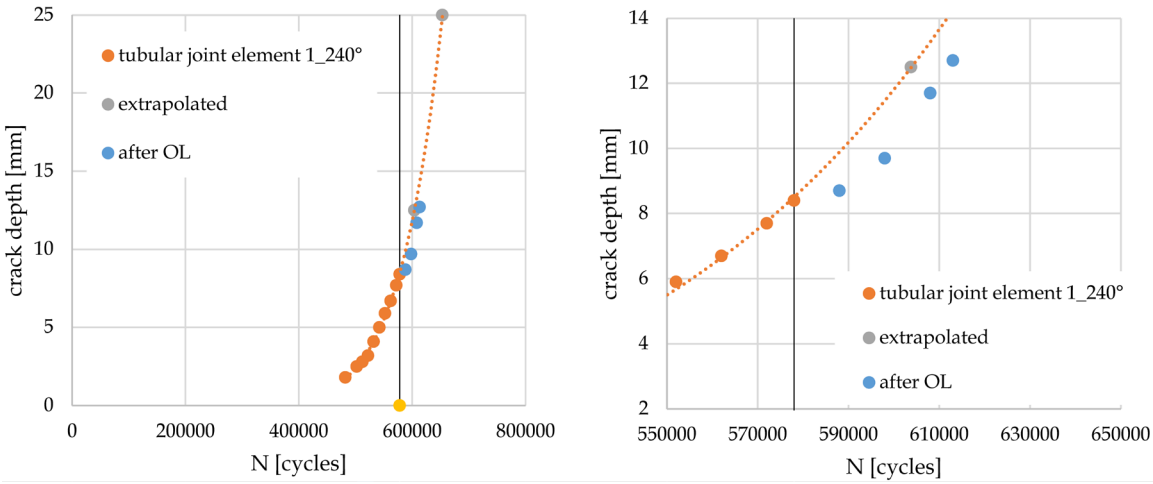

Figure 38: Measured crack depth before and after an OL (A_{OL} = 1.3) in tubular joint element 1

growth rate was limited, so the growth rate is an average over a crack extension of various millimetres. This explains the larger step size as compared to the coupon specimens.

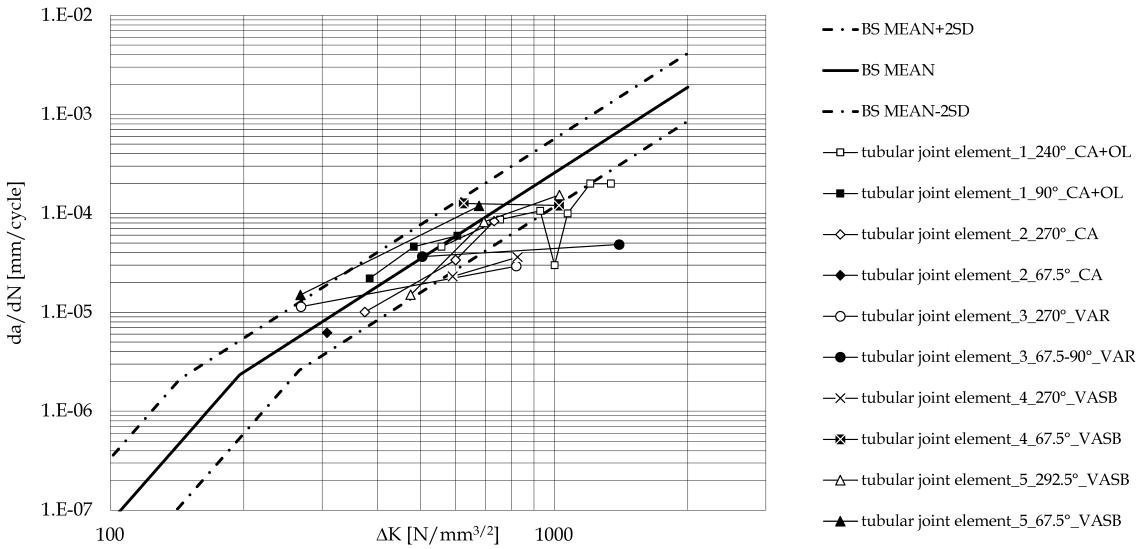

Crack growth rate according to BS7910:2019

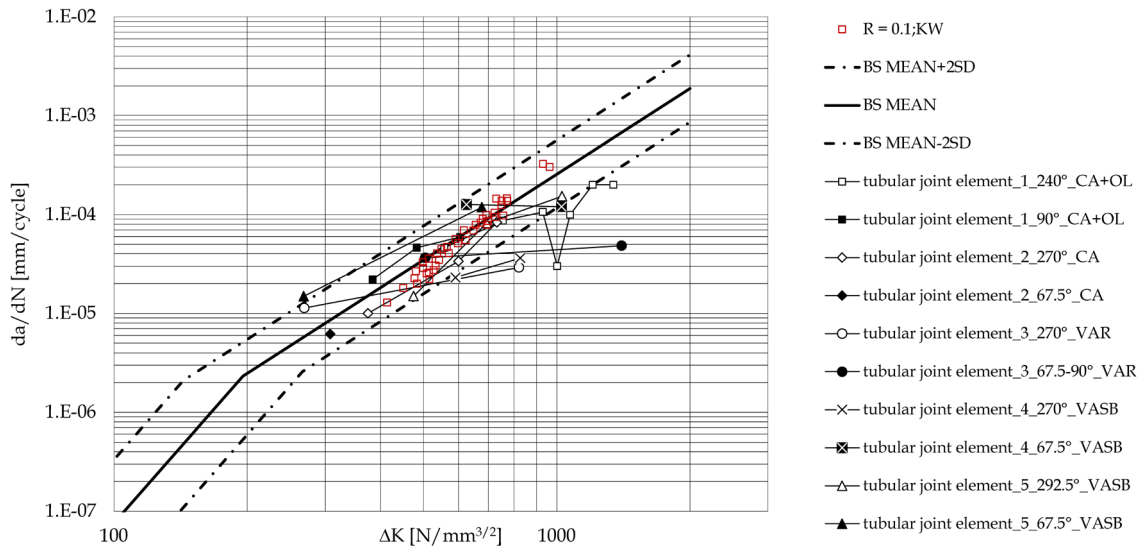

Crack growth rate compared with additionally the coupon specimens

Figure 39: Crack growth rate as measured in tubular joint elements

The crack growth rates as observed in the tubular joint elements is within the BS7910:2019 scatter band up to stress intensity factor of approximately 700 N/mm$^{3/2}$. A lower crack growth rate as compared to BS7910:2019 is observed at deeper cracks in the tubular joint elements. This is attributed to a load shedding effect, where the crack tips enter a zone of lower stress range as they move away from the saddle point, see Figure 34b combined with Figure 37. This also implies that the procedure to estimate the stress intensity factor is conservative for deeper cracks. The effects of overloads in tubular joint element 1 is clearly visible. The fact that the crack sizes were recorded at discrete cracks and not continuously implies that the lowest rate after the overload is probably not recorded, hence the actual effect of OL's is even larger than displayed. Qian et al. (2012) studied single overloads in tubular joints and report that the single overloading event delays the propagation of the fatigue surface cracks near the weld toe along the brace-to-chord intersection in the large-scale X-joint specimen. However, the retardation effect caused by the overload depends on the depth of the fatigue crack. A deep fatigue crack experiences more significant delays in the fatigue crack propagation caused by the overload than does a shallow fatigue crack, which is confirmed by the current study. On the contrary, Dover & Holdbrook (1980) showed a crack growth acceleration effect as a result of an overload, most probably due to instantaneous brittle crack extension.

Relative to constant amplitude (CA) case, the crack growth rate at variable amplitude loading, both the random variable amplitude loading (VAR) and the variable amplitude block loading (VASB), have lower rate at deeper cracks. This may be explained by the fact that at deeper (and wider) cracks, no significant crack closure occurs as the crack flanks are plastically deformed.

3.6 Evaluation of S-N curves

Several standards and recommendations give S-N curves for tubular joint elements: DNVGL-RP-C203:2016, EN1993-1-9:2012, Hobbacher (2016), Zhao et al. (2001), ISO14347:2008 and API RP 2A-WSD:2012. DNVGL-RP-C203:2016 adopts the hot spot stress approach and includes specific stress concentration factors for tubular joint elements and is typically applied in the evaluation of offshore wind turbine components. For this reason, the test data were compared to the S-N curves in DNVGL-RP-C203:2016.
Given the relatively small number of data, the constant amplitude and variable amplitude loading data were combined in the statistical evaluation for failure criterion $N_{0.5t}$. The characteristic strength is evaluated at 75% confidence level of 97,7% probability of survival,

with fixed slope m = 3. In addition to the evaluation with unknown prior standard deviation as given in section 2.5, a known prior standard deviation s = 0.2 was assumed in line with DNVGL-RP-C203:2016. Table 15 lists the results of the statistical evaluation. For comparison, the fatigue strength values of DNVGL-RP-C203:2016 were also listed in the table. Figure 40 shows the experimental data and resulting S-N curves based on the statistical evaluation, compared to characteristic strengths presented in DNVGL-RP-C203:2016.

Table 15: S-N results in comparison with DNVGL-RP-C203:2016

	CA and VASB	VAR	DNVGL RP (2016) Cat. T
N	9 samples	2 samples	
M	3	3	
Log b	12.44	12.15	
At $N = 10^7$:			
$\Delta\sigma_{MEAN}$ [MPa]	64.9	52	81.6*
s known a priori			
s	0.2		0.2
$\underline{k}$	2.22		2
Log(b – ks)	11.99		
At $N = 10^7$:			
$\Delta\sigma_{MEAN\text{-}2s}$ [MPa]	46.1		60.0*
s unknown a priori			
s	0.07		
k	3.76		
Log(a – ks)	12.16		
At $N = 10^7$:			
$\Delta\sigma_{MEAN\text{-}2s}$ [MPa]	52.6		60.0*

*including thickness effect

The standard deviation in terms of N of the tubular joint element tests is s = 0.07. The characteristic (MEAN-2s) S-N curves obtained from the data for unknown and known standard deviation are below the characteristic S-N curves of DNVGL-RP-C203:2016. It appears that the MEAN S-N curve from the tests is lower (i.e. providing a shorter life) than DNVGL-RP-C203:2016.

The lives of CA tests with CA+OL and block loads VASB are in the same scatter band as the life of the CA test. The results of the VAR test are evaluated separately from the other tubular joint element tests. The VAR tests with random loading provide a slightly shorter

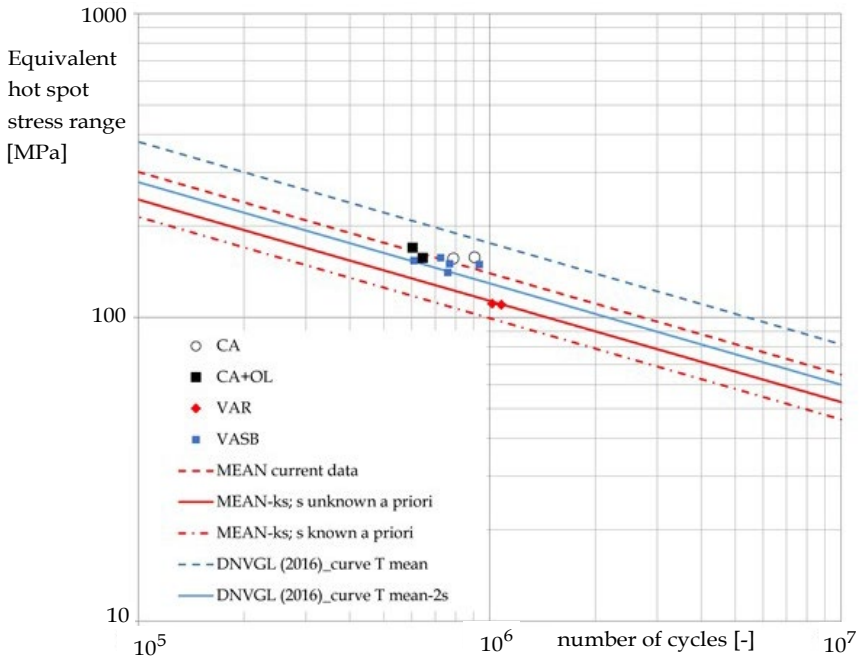

Figure 40: S-N curve of tubular joint elements based on equivalent hot spot stresses

life as compared to the CA data (mean – 1.43**s*, with *s* = 0.2). This is in contradiction with the crack growth evaluation of the tubular joint and the coupon tests, from which a similar crack growth life between CA the VAR and VASB tests was observed for small cracks, and a relatively lower crack growth rate at deeper cracks was observed in the VAR and VASB tests. The difference is attributed to crack initiation or growth of very shallow cracks, present in the evaluation of Figure 40 but not in the other data. Crack closure due to crack flank contact cannot take place at these initial stages and the crack growth between load events is so small that retardation due to crack closure cannot take place. In addition, residual stresses are high in this region, further limiting the possibilities of crack closure. The high elastic peak stress near the weld obtained through the FE method toe in Figure 35 in combination with VA may result into cyclic plasticity during the largest cycles, thereby shortening the life at particularly small crack sizes that are governing for the total fatigue life. Zhang & Maddox (2009) also found a significant difference between CA and VA loading on the total life of a welded joint (with simpler geometry than the one considered here).

The current study shows that load sequence effects that are usually investigated through simple geometries on base metal, are less pronounced for the total life but more pronounced for large cracks in realistic welded joints.

4 Conclusions

Aim of the current paper is to assess load sequence effects in coupon specimens that are usually considered for this purpose and tubular joint element specimens with realistic loading as obtained in practical conditions.

The coupon specimen experiments performed in this research have resulted into detailed and accurate values of crack growth rates for the materials investigated, being S355G10+M and S460M. The difference in steady state crack growth rate between the two materials is insignificant. The stress ratio dependency of the crack growth rate was investigated. The experiments indicated that the crack growth rate increases with increasing stress ratio, which confirms literature findings, but the effect is less pronounced as in other research on similar steels. The minimum stress was equal to the opening stress – i.e. no crack closure – at stress ratios of 0.6 or 0.7. Pivot points, i.e. distinct stress intensity factor values at which a change in slope of the crack growth rate function was observed, were observed which led to four zones with different parameters of Paris' equation. These different zones could not be linked to differences in metallurgical or fractographic characteristics.

Bead-on-plate welds (single weld run) and K-welds (weld over full member thickness) were tested using base materials S355G10+M and S460 and matching filler material. Tensile residual stresses present in the outer fibre of the specimens raise the effective stress ratio R. The material parameters to determine the crack growth rate of the welded material match the parameters obtained for $R > 0.6{\sim}0.7$ in the base material tests, i.e. the regime without crack closure.

For all materials and conditions, the experiments performed indicate that overloads shortly increase the crack growth rate directly following the overload and after that the crack growth rate reduces over a longer period. The combined net effect is crack growth retardation, similar to the findings of others. The effect of retardation in terms of additional number of cycles is correlated to the ratio of the maximum stress of the overload and the maximum stress of the other cycles and the crack size, and it is weakly correlated to the

stress range of the overload and the maximum stress of the other cycles. Load sequence influence on the crack growth rates are also observed in case of subsequent blocks of constant amplitude loading with different mean stress. An underload causes crack growth acceleration. However, the acceleration is smaller as compared to retardation following an overload. A more dominant effect of an underload is that it reduces or even cancels the retarding effect of an overload. In case of a randomised variable amplitude loading, the average crack growth rate was in line with that of CA loading.

To make the step towards a realistic welded joint, a test program was set up comprising of six full scale tubular joint elements with S355J2H and S355G13+N as brace and chord material, respectively. Such joints are used in the jackets of offshore wind turbines. Typically, in the tubular joint elements, crack initiation took place at various locations close to the two saddle positions and the cracks at each saddle position coalesced to form one dominant crack during fatigue loading. Strain measurements and simulations have provided insight into the hot spot stress ranges around the perimeter of these joints.

The current study shows that load sequence effects, which are usually investigated through simple geometries on base metal, are less pronounced for the total life but more pronounced for the residual life of deep cracks in realistic welded joints.

Acknowledgements

This project was sponsored by the TKI Wind op Zee. The authors would like to thank the project partners OCAS, Keppel Verolme, VGB and Noordzeewind. Furthermore, the authors thank Arcelor Mittal and Salzgitter Mannesmann for sponsoring test material and Keppel Verolme for manufacturing the tubular joint element specimens. Finally, the authors thank Erik Schuring for facilitating the microscopic evaluation at TNO Energy Transition.

References

Alderliesten, R.C. (2016). How proper similitude can improve our understanding of crack closure and plasticity in fatigue,. *International Journal of Fatigue*, 82:263-273

Amsterdam, E. & Grooteman, F. (2016). The influence of stress state on the exponent in the power law equation of fatigue crack growth. *International Journal of Fatigue*, 82:572-578

API RP 2A-WSD: 2012 Recommended Practice for Planning, Designing and Constructing Fixed Offshore Platforms—Working Stress Design. American Petroleum Institute.

ASTM E647-15e1:2015 Standard test method for measurement of fatigue crack growth rates. ASTM International

Bacila, A, Decoopman, X, Mesmacque, G, Voda, M. & Serban, V.A. (2007). Study of underload effects on the delay induced by an overload in fatigue crack propagation. *International Journal of Fatigue*, 29:1781-1787

Booth, G. S., & Maddox, S. J. (1988). Correlation of fatigue crack growth data obtained at different stress ratios. Mechanics of Fatigue Crack Closure. ASTM International

Borrego, L.P., Ferreira, J.M., Pinho da Cruz, J.M. & Costa, J.M. (2003). Evaluation of overload effects on fatigue crack growth and closure. *Engineering Fracture Mechanics*, 70:1379-1397

BS7910:2019 Guide on methods for assessing the acceptability of flaws in metallic structures. British Standards Institute

De Jesus, A.M.P., Matos, R., Fontoura, B.F.C., Simões da Silva, L. & Veljkovic, M. (2012), A comparison of the fatigue behavior between S355 and S690 steel grades. *Journal of Constructional Steel Research*, 79:140-150

DNVGL-RP-C203:2016 Fatigue design of offshore steel structures. DNV GL.

Dover, W.D. & Holdbrook, S.J. (1980). Fatigue crack growth in tubular welded connections. *International Journal of Fatigue*, 2:37-43

Dragt, R.C., Hengeveld, S.T., Maljaars, J. (2020). A new analytical approach for describing fatigue load sequence effects, *HERON* Vol. 65 No. 1/2, p. 109-149.

Efthymiou, M. (1988). Development of SCF formulae and generalized functions for use in fatigue analyses. OTJ'88, Surrey, UK

EN1993-1-9:2012 Design of steel structures - General - Part 1.9: Fatigue strength of steel structures. European Committee for Standardization

European Convention for Constructional Steelwork (2018), Background information on fatigue design rules: statistical evaluation, 2nd ed.

Fisher, J.W., Mertz D.R. & Zhong A. (1983). Steel bridge members under variable amplitude, long life fatigue loading. Report No. 463-1(83). Fritz Engineering Laboratory Lehigh University

Fitnet (2008). Fitness-for-Service (FFS) - Procedure (Volume 1) ISBN 978-3-940923-00-4, Koçak, M., Webster, S., Janosch, J.J., Ainsworth, R.A., Koers, R., printed by GKSS Research Center, Geesthacht.

Forman, R. G., & Mettu, S. R. (1992). Fracture mechanics: 22nd symposium, Philadelphia. In D. M. A Saxena HA Ernst (Ed.), Behavior of surface and corner cracks subjected to tensile and bending loads in Ti–6Al–4V alloy (pp. 519–46). ASTM STP 1131

Hobbacher, A. (2016). *Recommendations for Fatigue Design of Welded Joints and Components* XIII-1965-03 / XV-1127-03. International Institute of Welding.

ISO12108:2012 Metallic materials - Fatigue testing - Fatigue crack growth method. International Organisation for Standardization

ISO14347:2008 Fatigue – Design procedure for welded hollow-section joints – Recommendations. International Organisation for Standardization

ISO19902:2007 Petroleum and natural gas industries – Fixed steel offshore structures. International Organisation for Standardization

Iwasaki, T., Kawahara, M., & Asano, K. (1979). Fatigue crack growth behavior in welded tubular joints in T, TY and K. Offshore Technology Conference. Offshore Technology Conference

Kurihara, M., Katoh, A. & Kawahara, M. (1987). Effects of Stress Ratio and Step Loading on Fatigue Crack Propagation Rate. Current Research on Fatigue Cracks, *Current Japanese Materials Research*, 1:247–265

Lim, J. K. & Stephens R. I. (1990), Fatigue crack growth and retardation in the welded HAZ of 4140 steel. Welding Research Supplement; 1:294s–304s

Lotsberg, I. (2014). Assessment of the size effect for use in design standards for fatigue analysis. *International Journal of Fatigue*, 66:86–100

Lu, Y-c, Yang, F-p & Chen, T (2019). Effect of single overload on fatigue crack growth in QSTE340TM steel and retardation model modification. *Engineering Fracture Mechanics*, 212:81-94

Maddox, S. J. & Andrews, R. M. (1990). Stress intensity factors for weld toe cracks. In: Aliabada, M.H., Brebbia, C.A. and Cartwright, D.J. (eds). *Localized damage computer-aided assessment and control*. Portsmouth, UK

Maljaars, J. & Tang, L. (2020). How the finite element method helps explaining fatigue, crack growth retardation and acceleration. *HERON* Vol. 65 No. 1/2, p. 69-108.

Maljaars, J., Pijpers, R. & Slot, H. (2015). Load sequence effects in fatigue crack growth of thick-walled welded C–Mn steel members. *International Journal of Fatigue*, 79:10–24

Matelect. (2014). *The Potential Drop Technique & Its Use in Fatigue Testing*. London: Matelect LTD

Mohanty, J.R., Verma, B.B. & Ray, P.K. (2009). Prediction of fatigue crack growth and residual life using an exponential model: Part II (mode-I overload induced retardation). *International Journal of Fatigue*, 31:425-432

Newman J.C. Jr. (1981). A crack-closure model for predicting fatigue crack growth under aircraft spectrum loading. In: *Methods and models for predicting fatigue crack growth under random loading*, ASTM STP 748. pp. 53–84

Newman J.C. Jr. (1982). Prediction of fatigue crack growth under variable-amplitude and spectrum loading using a closure model. In: *Design of fatigue and fracture resistant structures*, ASTM STP 761; pp. 255–77

Newman J.C. jr. (1984). A crack opening stress equation for fatigue crack growth. *International Journal of Fracture*, 24:R131–5

Noordhoek C. (1997), Fatigue and fracture behaviour of welded joints in high strength steels (FeE460). Report EUR 17816 en. Brussels: ECSC

Overbeeke, J. L., & Back, J. de. (1987). The influence of stress relieving and R-ratio on the fatigue of welded joints. In S. Maccos (Ed.), *Fatigue of welded constructions* (pp. 11–22). Brighton: The Welding Institute

Qian, X., Swaddiwudhipong, S., Nguyen, C.T., Petchdemaneengam, Y., Marshall, P & Ou, Z. (2012). Overload effect on the fatigue crack propagation in large-scale tubular joints. *Fatigue & Fracture of Engineering Materials & Structures*, 36:427–438

Rikken, M., Pijpers, R.J.M., Slot, H. & Maljaars, J. (2018). A combined experimental and numerical examination of welding residual stresses, *Journal of Materials Processing Technology*, 261:98-106

Rushton, P.A. & Taheri, F. (2003). Prediction of crack growth in 350 WT steel subjected to constant amplitude with over- and under-loads using a modified Wheeler approach. *Marine Structures*, 16:517-539

Salvati, E., Zhang, H., Fong, K.S., Song, X. & Korsunsky, A.M. (2017). Separating plasticity-induced closure and residual stress contributions to fatigue crack retardation following an overload. *Journal of the Mechanics and Physics of Solids*, 98:222-235

Sander, M. & Richard, H.A. (2006). Fatigue crack growth under variable amplitude loading Part I: experimental investigations. *Fatigue & Fracture of Engineering Materials & Structures*, 29:291–301

Schijve J, Skorupa M, Skorupa A, Machniewicz T & Gruszczynski P. (2004). Fatigue crack growth in the aluminum alloy D16 under constant and variable amplitude loading, *International Journal of Fatigue*, 26:1–15

Schijve J. (2009). *Fatigue of structures and materials*, 2nd ed. Springer Science+Business media B.V

Tada, H., Paris, P. C., & Irwin, G. R. (1973). *The stress analysis of cracks*. Handbook, Del Research Corporation

Tanaka, K. (1989). *Mechanics and Micromechanics of Fatigue Crack Propagation*. ASTM STP 1020, American Society for Testing and Materials, Philadelphia, PA, 151–183

Vosikovsky, O. (1975). Fatigue-crack growth in an X-65 line-pipe steel at low cyclic frequencies in aqueous environments. *Journal of Engineering Materials and Technology*, 97(4), 298–304

Yamada, Y., Ziegler, B. & Newman Jr., J.C. (2011). Application of a strip-yield model to predict crack growth under variable-amplitude and spectrum loading – Part 1: Compact specimens, *Engineering Fracture Mechanics*, 78:2597–2608

Yuen, B.K.C. & Taheri, F.(2006). Proposed modifications to the Wheeler retardation model for multiple overloading fatigue life prediction. *International Journal of Fatigue*, 28:1803-1819

Zhang, Y. & Maddox, S. J. (2009). Investigation of fatigue damage to welded joints under variable amplitude loading spectra. *International Journal of Fatigue*, 31:138-152

Zhao, X., Herion, S., Packer, J., Puthli, R., Sedlacek, G., J. Wardenier, & Yeomans, N. (2001). *Design Guide for circular and rectangular hollow section welded joint under fatigue loading*. CIDECT

Zheng X, Lü B, Cui T, Lü X. & Lin C. (1994). Fatigue tests and life prediction of 16 Mn steel butt welds without crack-like defect. *International Journal of fracture*, 68:275–85.

Zitounis, V. & Irving, P.E. (2007). Fatigue crack acceleration effects during tensile underloads in 7010 and 8090 aluminum alloys. *International Journal of Fatigue*, 29:108-118

Annex A Forman Mettu Approach

The Forman & Mettu (1992) approach is followed for the calculation of U, which is a function of R, but also of the material's mechanical strength, stress condition and maximum stress:

$$U = \frac{1 - f_{K_{op}K_{max}}}{1 - R} \tag{A-1}$$

where:

$$R = \frac{F_{min}}{F_{max}}$$

$$f_{K_{op}K_{max}} = \begin{cases} \max(0, R, f_1) & if\ R > 0 \\ \max(0, f_2) & if\ R \leq 0 \end{cases}$$

$$f_1 = A_0 + A_1 R + A_2 R^2 + A_3 R^3$$

$$f_2 = A_0 + A_1 R$$

$$A_0 = (0.825 - 0.34\alpha_1 + 0.05{\alpha_1}^2)\left(\cos\left(\frac{\pi s_{max} s_0}{2}\right)\right)^{1/\alpha_1}$$

$$A_1 = (0.415 - 0.071\alpha_1) s_{max} s_0$$

$$A_2 = 1 - A_0 - A_1 - A_3$$

$$A_3 = 2A_0 + A_1 - 1$$

$$s_{max} s_0 = \left|\frac{s_{max}}{s_0}\right|$$

$$s_{max} = \frac{1}{4}\left|\frac{F_{max}}{2}\right| l_0 \frac{1000}{S}$$

$$s_0 = \frac{f_y + f_u}{2}$$

$$K_{max} = \frac{\Delta K}{1 - R} \tag{A-2}$$

$$K_{op} = f_{K_{op}K_{max}} \cdot K_{max}$$

$$sc_{factor} = \sqrt{\frac{a}{a + asc_0}}$$

$$\Delta K_{th} = \begin{cases} \Delta K_0 \cdot sc_{factor} \cdot \left(\frac{1 - A_0 \cdot (1 - R)}{1 - f_{K_{op}K_{max}}}\right)^{(1+C_{thn} \cdot R)} & if\ R < 0 \\ \Delta K_0 \cdot sc_{factor} \cdot \left(\frac{1 - A_0 \cdot (1 - R)}{1 - f_{K_{op}K_{max}}}\right)^{(1+C_{thp} \cdot R)} & if\ 0 \leq R < R_{cl} \\ \Delta K_0 \cdot sc_{factor} \cdot \left(\frac{1 - A_0 \cdot (1 - R_{cl})}{1 - f_{K_{op}K_{max}}}\right)^{(1+C_{thp} \cdot R)} & if\ R \geq R_{cl} \end{cases}$$

$$\Delta K_{eff} = K_{max} - K_{op}$$

$$\frac{da}{dN} = \begin{cases} 10^{-100}\ if\ \Delta K_{eff} < \Delta K_{th} \\ A_p \cdot {\Delta K_{eff}}^m \cdot \frac{\left(1 - \frac{\Delta K_{th}}{\Delta K_{eff}}\right)^p}{\left(1 - \frac{K_{max}}{K_{1C}}\right)^q}\ otherwise \end{cases}$$

Table A1: Best fit Forman Mettu parameters

f_y = 380 MPa	α_1 = 2.5 [-]
f_u = 486 MPa	K_{1C} = 18500 N/mm$^{3/2}$
ν = 0.3 [-]	a_{sc0} = 0.0381 mm
ΔK_0 = 200 N/mm$^{3/2}$	C_{thn} = 1 [-]
p = 0.2 [-]	C_{thp} = 2 [-]
q = 1 [-]	R_{cl} = 0.75 [-]

Annex B Material parameters and load sequence results

Table B1: Material parameters crack growth rate; index 1: first part of bi-linear (log) relation; index 2: second part of bi-linear (log) relation

Fig.	Specimen series		*m1*	$C1_{mean}$	$C1_{mean+sd}$	*s1*	*m2*	$C2_{mean}$	$C2_{mean+sd}$	*s2*
10a	BM35	ΔK_{eff}	3.60	8.06E-15	1.22E-14	0.18	2.23	6.57E-11	7.53E-11	0.06
11a	BM35+BM46	ΔK_{eff}	3.66	6.06E-15	8.92E-15	0.17	2.46	1.83E-11	2.18E-11	0.08
11b	BM46	ΔK_{eff}	3.71	4.68E-15	6.25E-15	0.13	2.29	5.41E-11	6.61E-11	0.09
12a	BM35+BM46	ΔK	2.88	5.51E-13	1.35E-12	0.19				
12b	BM35+BM46	ΔK	2.88	4.58E-13	1.03E-12	0.18				
13a	BM35+BM46+BP35+ BP46	$\Delta K = \Delta K_{eff}$	2.88	5.01E-13	1.16E-12	0.18				
14a	BM35+BM46+BP35+ BP46+KW35+KW46	$\Delta K = \Delta K_{eff}$	2.88	4.80E-13	1.12E-12	0.18				

Table B2: Coupon specimen details

Specimen Series	Name	Loading	Stress relieved	Width W	Height B	Outer span Supports L_o	Inner span Supports L_i	a_i Side 1	a_i Side 2
	[-]		[N.A./yes/no]	[mm]	[mm]	[mm]	[mm]	[mm]	[mm]
BM35	BM0135	Table B3	N.A.	25.0	50.0	200	100	0.44	0.58
BM35	BM0235	Table B3	N.A.	25.0	50.0	200	100	0.51	0.53
BM35	BM0335	CA	N.A.	25.0	50.0	202	100	0.25	0.25
BM35	BM0835	Table B3	N.A.	25.0	50.0	202	99	1.83	1.90
BM35	BM0935	CA	N.A.	25.0	50.0	282	140	1.82	1.85
BM35	BM1035	CA	N.A.	25.0	50.0	280	141	1.85	1.85
BM35	BM1135	CA	N.A.	25.0	50.0	280	140	2.23	2.07
BM35	BM1235	Table B3	N.A.	25.0	50.0	280	140	1.90	1.89
BM35	BM1335	CA	N.A.	25.0	50.0	280	140	2.12	2.02
BM35	BM1435	VAR	N.A.	25.0	50.0	282	141	2.00	1.90
BM35	BM1535	Table B3	N.A.	25.0	50.0	280	140	1.90	1.90
BM35	BM1635	Table B3	N.A.	25.0	50.0	280	140	2.25	2.25
BM35	BM1735	Table B3	N.A.	25.0	50.0	280	140	2.25	2.25
BM35	BM1835	CA	N.A.	25.0	50.0	280	140	2.27	2.27
BM35	BM1935	CA	N.A.	25.0	50.0	280	140	2.0	2.0
BM35	BM2435	CA	N.A.	25.0	50.0	280	140	2.0	2.0
BM35	BM2535	Table B3	N.A.	25.0	50.0	280	140	2.10	2.10
BM35	BM2635	CA	N.A.	25.0	50.0	280	140	2.05	2.06
BM46	BM0146	Table B3	N.A.	20.0	40.0	200	100	1.80	1.80
BM46	BM0246	Table B3	N.A.	20.0	40.0	200	100	1.80	1.75
BM46	BM0346	Table B3	N.A.	20.0	40.0	200	100	1.83	1.94
BM46	BM0446	CA	N.A.	20.0	40.0	200	100	1.82	1.87
BM46	BM0546	VAR	N.A.	20.0	40.0	200	100	2.00	2.08
BM46	BM0646	CA	N.A.	20.0	40.0	200	100	1.81	1.82
BP35	BP0135	Table B3	no	25.0	50.3	201	100	0.54	0.55
BP35	BP0235	Table B3	no	25.1	50.2	199	100	0.58	0.60
BP35	BP0335	CA	no	25.2	50.2	200	100	0.69	0.93
BP35	BP0435	Table B3	no	25.0	50.1	200	100	0.98	0.90
BP35	BP0535	Table B3	yes	25.1	50.2	200	100	1.87	2.12
BP35	BP0635	Table B3	no	25.1	49.5	280	140	1.85	1.89
BP35	BP0735	Table B3	no	25.3	49.8	280	140	0.71	0.93
BP35	BP0935	VAR	no	25.1	50.0	280	140	0.00	0.00
BP46	BP0146	Table B3	no	19.4	38.6	200	100	2.05	2.10
BP46	BP0246	Table B3	no	20.0	40.0	200	100	2.05	1.92
KW35	KW0135	Table B3	no	25.1	49.6	200	99	1.36	0.61
KW35	KW0335	Table B3	no	25.0	49.6	200	100	2.30	2.20
KW35	KW0435	Table B3	no	25.0	49.7	200	100	1.81	1.83
KW46	KW0146	Table B3	no	19.2	38.9	200	100	2.12	2.11
KW46	KW0246	Table B3	no	19.5	38.8	200	100	2.56	2.47

Table B3: Load sequence results coupon specimens

Specimen	*Sequence*	*N1*	*a/T*	*R*	D_{sl} or D_{ul}	A_{sl}	f_{daldN}	*Zone*	*Specimen*	*Sequence*	*N1*	*a/T*	*R*	D_{sl} or D_{ul}	A_{sl}	f_{daldN}	*Zone*
BM0135	OL	143343	0.06	0.1	1.76	1.69	8.2	'3'	BP0435	OL	97070	0.07	0.1	1.31	1.29	1.4	'3'
BM0135	OL	210657	0.09	0.1	1.76	1.69	4.7	'3'	BP0435	MCD	106883	0.10	0.1	1.25	1.25	1.4	'3'
BM0135	UL	241516.5	0.12	0.5	1.96	1	0.9	'1'	BP0435	MCD	123642	0.13	0.1	1.24	1.25	0.8	'2'
BM0135	UL	304985	0.17	0.5	1.96	1	0.6	'2'	BP0435	MCU	139063	0.15	0.1	0.8	0.8	0.4	'4'
BM0135	OL+UL	317553	0.20	0.5	2.72	1.38	2.0	'2'	BP0435	MCU	141764	0.18	0.3	1.03	0.8	0.7	'4'
BM0235	OL	163003	0.05	0.1	1.78	1.7	5.1	'2'	BP0435	MCD	148014	0.22	0.3	1.17	1.18	2.3	'3'
BM0235	OL	255047	0.09	0.1	1.78	1.7	4.9	'3'	BP0535	OL	205973	0.08	0.3	1.42	1.3	0.8	'1'
BM0835	MCU	1410508	0.06	0.2	1.19	1.01	1.0	'1'	BP0535	MCD	326546	0.13	0.1	1.25	1.25	0.5	'1'
BM0835	MCD	10646757	0.28	0.5	0.58	0.99	0.7	'1'	BP0535	MCU	402136	0.19	0.3	0.82	0.64	0.8	'3'
BM1235	OL+UL	304875.5	0.07	0.3	3.4	2.01	2.9	'1'	BP0535	MCD	428700	0.24	0.3	1.19	1.14	0.8	'2'
BM1235	OL+UL	633104.5	0.11	0.3	3.11	1.81	2.8	'2'	BP0735	MCU	13377	0.04	0.3	1.29	1	0.8	'1'
BM1235	OL	815001	0.16	0.2	1.53	1.44	4.1	'1'	BP0735	OL	71902	0.07	0.3	1.42	1.3	1.9	'2'
BM1535	OL	473317	0.12	0.3	1.95	1.66	3.7	'2'	BP0735	MCD	107577	0.09	0.1	0.97	1.25	1.7	'2'
BM1535	OL	594145	0.14	0.3	1.95	1.66	3.4	'2'	BP0735	MCD	124321	0.12	0.1	1.25	1.26	0.9	'2'
BM1635	OL	59516	0.07	0.3	1.4	1.29	1.9	'2'	BP0735	MCU	146673	0.16	0.1	0.8	0.8	0.7	'4'
BM1635	MCD	84038	0.10	0.1	0.97	1.25	2.5	'3'	BP0735	MCU	150877	0.19	0.3	1.03	0.8	1.0	'4'
BM1635	MCD	107503	0.13	0.1	1.25	1.25	2.0	'2'	BP0735	MCD	154451	0.21	0.3	1	1	1.7	'4'
BM1735	OL	70483	0.08	0.3	1.42	1.3	2.2	'2'	BP0735	MCD	161414	0.23	0.3	1	1	1.5	'3'
BM1735	MCD	99046	0.10	0.1	0.97	1.24	2.1	'3'	BP0146	MCU	336004	0.11	0.5	1.27	0.89	0.6	'1'
BM1735	MCD	125383.5	0.13	0.1	1.24	1.25	1.9	'2'	BP0146	MCD	2728066	0.36	0.5	0.58	0.99	0.5	'2'
BM1735	MCU	155194	0.16	0.1	0.8	0.8	0.6	'4'	BP0246	OL	52949	0.09	0.3	1.43	1.3	0.9	'2'
BM1735	MCU	158977	0.19	0.3	1.03	0.8	0.8	'4'	BP0246	MCD	70709	0.14	0.1	0.97	1.25	1.3	'3'
BM1735	MCD	163627.5	0.23	0.2	1.1	1.18	3.0	'4'	BP0246	MCD	76060	0.15	0.1	1.14	1.15	0.7	'3'
BM1735	MCD	170246	0.24	0.3	1.05	1.04	1.8	'4'	BP0246	MCD	85611.5	0.19	0.1	1.18	1.14	0.6	'2'
BM1735	MCD	173291	0.25	0.3	1.19	1.14	1.1	'4'	BP0246	MCU	92669	0.22	0.1	0.8	0.8	0.6	'4'
BM2535	OL	468911	0.12	0.3	1.95	1.67	9.4	'1'	BP0246	MCD	97951	0.27	0.3	1.18	1.18	1.1	'4'
BM2535	OL+UL	604619	0.13	0.3	2.34	1.68	1.8	'2'	BP0246	MCD	102000	0.29	0.3	1.18	1.18	1.2	'4'
BM0146	OL	518115	0.15	0.3	1.92	1.67	2.3	'2'	KW0135	OL	205433	0.09	0.1	1.74	1.68	3.3	'3'
BM0146	OL	597717	0.17	0.3	1.95	1.67	2.6	'2'	KW0135	MCD	222486	0.13	0.5	1.99	1.11	0.8	'2'
BM0246	MCU	22552	0.05	0.3	1.3	1	0.8	'1'	KW0135	MCD	254277	0.18	0.2	1.13	1.79	6.4	'2'
BM0246	OL	81990	0.08	0.3	1.44	1.3	1.0	'2'	KW0335	OL	512030	0.13	0.3	1.92	1.66	2.5	'2'
BM0246	MCU	155000	0.19	0.1	0.8	0.8	1.1	'4'	KW0335	OL	570803	0.15	0.3	1.92	1.66	2.4	'2'
BM0246	MCD	174532.5	0.29	0.3	0.63	1.18	2.0	'4'	KW0435	MCU	54029	0.04	0.3	1.16	0.96	0.9	'1'
BM0346	MCU	27831	0.05	0.3	0.23	0.73	0.8	'1'	KW0435	OL	242312	0.07	0.3	1.42	1.3	0.9	'1'
BM0346	OL	81206.5	0.09	0.3	0.42	1.3	1.3	'2'	KW0435	MCD	345379	0.12	0.1	0.6	1.07	0.6	'1'
BM0346	MCD	108665	0.12	0.1	0.97	1.25	2.1	'2'	KW0435	MCU	444587	0.18	0.3	0.82	0.64	1.1	'3'
BM0346	MCD	133612	0.15	0.1	1.26	1.25	1.7	'2'	KW0435	MCD	472767	0.23	0.3	1	1	0.8	'2'
BM0346	MCU	172798	0.21	0.1	0.8	0.8	0.8	'4'	KW0246	MCU	11852	0.07	0.3	1.2	0.97	1.0	'2'
BM0346	MCD	187710	0.29	0.3	1.17	1.18	1.3	'3'	KW0246	OL	42157	0.10	0.3	1.41	1.3	1.8	'3'
BP0135	OL	370153.5	0.04	0.1	1.76	1.69	1.4	'1'	KW0246	MCD	71129	0.16	0.1	1.25	1.25	0.9	'2'
BP0235	OL	338135.5	0.06	0.1	1.75	1.69	1.7	'3'	KW0246	MCU	89785	0.21	0.1	0.8	0.8	0.8	'4'
BP0235	MCDU	373997	0.11	0.5	2	1.11	0.4	'2'	KW0246	MCU	93005	0.24	0.3	1.03	0.8	1.0	'4'
BP0235	UL	424428.5	0.14	0.5	1.94	0.99	0.3	'2'	KW0246	MCD	98530	0.29	0.3	1.18	1.18	1.3	'4'
BP0235	OL+UL	432148	0.16	0.5	2.7	1.38	1.1	'2'	KW0246	MCD	102918	0.31	0.3	1.18	1.18	1.3	'4'

OL=Overload; MCD = Mean change down; MCU = mean change up; UL = underload

Table B4: Zonal evaluation of the crack growth rate

Zone	**Crack growth rate number of data points**	**crack growth exponent**	**MEAN_crack growth constant**	**MEAN+SD_crack growth constant**	**MEAN-SD_crack growth constant**	**Standard deviation**
Zone 1	386	3.02	1.945E-13	2.992E-13	1.264E-13	0.09
Zone 2	234	6.12	9.847E-22	1.682E-21	5.764E-22	0.12
Zone 3	234	3.14	1.939E-13	2.861E-13	1.314E-13	0.08
Zone 4	279	2.38	3.084E-11	4.451E-11	2.137E-11	0.08

Table B5: Location of pivot points

Zone	**Pivot points**					
	MEAN		**MEAN+SD**		**MEAN-SD**	
	ΔK_{eff}	*da/dN*	ΔK_{eff}	*da/dN*	ΔK_{eff}	*da/dN*
	[N/mm$^{3/2}$]	[mm/cycle]	[N/mm$^{3/2}$]	[mm/cycle]	[N/mm$^{3/2}$]	[mm/cycle]
Zone 1	240	2.943E-06	240	4.528E-06	240	1.913E-06
	467	2.191E-05	451	3.045E-05	483	1.576E-05
Zone 2	467	2.191E-05	451	3.045E-05	483	1.576E-05
	603	1.050E-04	574	1.329E-04	633	8.305E-05
Zone 3	603	1.050E-04	574	1.329E-04	633	8.305E-05
	750	2.081E-04	728	2.804E-04	772	1.544E-04
Zone 4	750	2.081E-04	728	2.804E-04	772	1.544E-04
	1300	7.693E-04	1300	1.110E-03	1300	5.330E-04